Formation of authigenic grey monazite: a marker of palaeo-thermal anomaly in very-low grade metamorphic rocks?

Johann Tuduri[1,2*], Olivier Pourret[3], Eric Gloaguen[1,2], Philippe Lach[1,2], Emilie Janots[4], Sébastien Colin[1], Jérôme Gouin[5], Matthieu Chevillard[1], Laurent Bailly[1]

[1] BRGM, F-45060 Orléans, France

[2] ISTO, UMR7327, Université d'Orléans, CNRS, BRGM, F-45071 Orléans, France

[3] UniLaSalle, AGHYLE, F-60026 Beauvais, France

[4] Univ. Grenoble Alpes, CNRS, IRD, IFSTTAR, ISTerre, 38000 Grenoble, France

[5] Pôle Avenia, F-64053 Pau, France

[*] Correspondence: j.tuduri@brgm.fr

Abstract

The reassessment of the rare earth element (REE) potential of France led us to investigate REE behaviour in black-shales belonging to the Middle Ordovician Angers-Traveusot formation from central Britany (France), with an emphasis on the formation of nodular grey monazite during the diagenetic and low-grade metamorphic evolution. Temperatures conditions and mass transfer underwent in the black shales were first characterized using rock geochemistry, rock-eval pyrolysis and by gradual changes of clay mineral crystallinity. Then, monazite texture, composition and U–Pb in-situ dating were determined and correlated with the diagenetic/anchimetamorphic conditions. In the Ordovician black shales, nodular monazite appears at the transition between the upper diagenesis and the anchizone metamorphic facies, at conditions between 140 and 250°C, in response to processes controlled by different proxies of competing influences such as the organic matter maturation, Fe oxide/hydroxide and clay transformation with fluid releasing. Monazite occurs mainly as elongated nodules, up to 2 mm in diameter that are mostly characterised by their grey colour due to abundance in host-rock mineral inclusions. Monazite nodules compositions are systematically low in Th and U contents but are zoned with Nd and middle REE rich cores surrounded by light REE-rich rims, with no evidence of inherited domains. More rarely, small grains of LREE-rich monazite are observed in late stage fractures. Monazite nodules were dated at *ca.* 405-400 Ma, which is proposed to record high heat flux responsible of the anchimetamorphic conditions recorded at the base of Angers-Traveusot formation. Late monazite-Ce were dated at *ca.* 385 and 350 Ma at the onset of the Variscan deformation.

Introduction

The rare earth elements (REE) are trace elements in most geological settings that are particularly useful for understanding a wide variety of geological processes because of their specific properties. For example, the solution and mineral properties of REE make these elements excellent probes of low temperature geochemical reactions and processes (Johannesson et al., 1997; Michard, 1989; Noack et al., 2014; Pourret and Tuduri, 2017; Rillard et al., 2019; Wood, 1990). Interest in the REE geochemistry comes from their systematic in chemical properties that often leads to fractionation in geochemical systems (Henderson, 1984). Indeed, REE are a group of 16 chemical metallic elements that are coherent in terms of ionic radius, charge that generally occur in the trivalent oxidation state and mineral site coordination (Henderson, 1984; Jones et al., 1996; Lipin and McKay, 1989). They include the whole lanthanides (from ^{57}La to ^{71}Lu) and yttrium usually assimilated to lanthanides. Depending on the specific configurations of electrons within each atom, REE are also commonly split into light rare earth elements (LREE: La-Nd), middle rare earth elements (MREE; Sm-Tb) and heavy rare earth elements (HREE; Dy-Lu). Yttrium (Y) may be considered as a HREE.

Monazite [(LREE to MREE, Ca, Th, Y)PO_4] is one of the most significant REE minerals for geochemistry and geochronology (Bea, 1996; Engi, 2017; Montel et al., 1996; Parrish, 1990; Poitrasson et al., 1996). It is a common accessory mineral observed in a wide variety of metamorphic and magmatic rock types and is stable from the anchizone metamorphism to the highest metamorphic conditions (*e.g.* Spear and Pyle, 2002). At the Earth's surface, monazite is resistant to weathering, as shown by its widespread occurrence as detrital mineral in sands and sandstones. Under greenschist and low temperature conditions more generally, fluids play a major role in monazite reactivity during both prograde and (or) retrograde metamorphic conditions (Janots et al., 2011; Janots et al., 2008; Rasmussen and Muhling, 2007; Read et al., 2002; Seydoux-Guillaume et al., 2012). However, in low-grade metamorphic and diagenetic conditions, the origin of monazite can be controversial and has variously been interpreted as detrital, diagenetic or metamorphic (Čopjaková et al., 2011; Evans and

Zalasiewicz, 1996; Milodowski and Zalasiewicz, 1991; Rosenblum and Mosier, 1983; Wilby et al., 2007). This is especially true for the enigmatic crystallisation of nodular grey monazite found in shales, palaeoplacer and placer deposits in France, Belgium, Portugal, Siberia, Spain, Taiwan, USA, United Kingdom, Iran and several African countries (Alipour-Asll et al., 2012; Burnotte et al., 1989; Cooper et al., 1983; Donnot et al., 1973; García-Tenorio et al., 2018; Milodowski and Zalasiewicz, 1991; Read et al., 1987; Rosenblum and Mosier, 1983; Salgueiro et al., 2020). Published results on the origin of nodular monazite have been largely based on the structure and chemistry of nodules recovered from placers (Cobert et al., 2015; Cooper et al., 1983; Donnot et al., 1973; Milodowski and Zalasiewicz, 1991; Read et al., 1987; Rosenblum and Mosier, 1983). Nodular monazite corresponds to millimetric grains that are grey to almost black due to the abundance of micro-inclusions mostly carbonaceous, and that commonly exhibits a nodular ellipsoidal morphology. In regards to its chemical composition, nodular monazite is usually enriched in MREE (mostly Eu-Gd) and low in Th and U (Alipour-Asll et al., 2012; Donnot et al., 1973; Rosenblum and Mosier, 1983). These peculiar features give nodular grey monazite (NGM) a special interest as they may be explored and operated, because of their low radioactive contents, for the REE a critical commodity, widely used in green technologies (Guyonnet et al., 2016).

The origin of NGM is still debated and may be associated with compactional dewatering during sedimentation or low-grade regional metamorphism (Burnotte et al., 1989; Čopjaková et al., 2011; Evans and Zalasiewicz, 1996; Milodowski and Zalasiewicz, 1991). The source of the REE at the origin of NGM crystallisation is also debated. It may be related to the desorption of REE adsorbed on the surface of clay or Fe oxides/hydroxides, the degradation of organic matter (OM), or the dissolution of detrital REE minerals including monazite as was described from greenschist-facies metasediments (Evans and Zalasiewicz, 1996; Janots et al., 2008; Lev et al., 1998; Milodowski and Zalasiewicz, 1991; Pourret and Tuduri, 2017; Rasmussen and Muhling, 2007). Nevertheless common features highlight the lack of thickening and prograde metamorphism where NGM occurs and temperature of crystallisation ranging from 200 to 350°C (i.e. very low grade to low grade metamorphic conditions).

By contrast, study focusing on the analysis of the distribution of NGM in sedimentary formations and its links with basin thermicity, fluid flows and geodynamic settings are lacking. The aim of this study is therefore to present and discuss the formation of NGM in the light of their distribution with respect to the tectono-metamorphic evolution of the geological domain where it occurs in order to propose mineral exploration proxies. Taking into account mineral and rock geochemistry, quantification of the diagenetic to metamorphic conditions using the illite crystallinity, geochronological constraints all together with the distribution of deformation gradient, a model of formation for NGM is thus proposed and discussed in light of their implications concerning REE behaviour during diagenesis and low-grade metamorphism.

1. Geological setting

The Armorican Massif (Fig. 1), part of the Ibero-Armorican arc in the Western European Variscan belt, comprises three main domains (Northern, Central and Southern Armorican domains) with different tectonic and metamorphic histories bounded by two major dextral wrench zones, the North and South Armorican Shear Zones (NASZ and SASZ, Ballèvre et al., 2009; Gumiaux et al., 2004; Jégouzo, 1980). Deformation in the Northern Armorican Domain mainly occurred in the Neoproterozoic; this domain was part of the upper brittle crust during the Variscan orogeny (Brun et al., 2001). The Central Armorican Domain (CAD), where NGM occurrences are widespread (Fig. 1), is mostly composed of an upper Neoproterozoic to lower Cambrian shale and greywacke basement covered by Palaeozoic silico-clastic sedimentary rocks (Ballèvre et al., 2009). The Southern Armorican domain corresponds to the internal metamorphic zones of the Variscan belt (Ballèvre et al., 2009), and recorded a late-Devonian to Carboniferous crustal thickening, followed by a late-Carboniferous extensional period with numerous leucogranite injections. Both extensional stage and pluton emplacement are coeval with strike-slip along the SASZ (Gapais et al., 2015). In the CAD, palaeozoic rocks mostly Ordovician in age are emplaced in response to the opening of the Rheic Ocean between Avalonia and Gondwana from about the late Cambrian (Ballèvre et al., 2009; Nance et al.,

2012). In the studied area (Figs. 1-3), the “Initial Red Beds” (Pont-Réan formation) give way to the Grès Armoricain formation dated as Floian (Lower Ordovician) and overlie unconformably the Neoproterozoic basement (Robardet et al., 1994). Formations are made up of quartz-arenites, however the upper part of the Lower Ordovician (UPLO) formation shows more important silty-clayey intercalations (Fig. 3). They record an important marine transgression with significant thickness variations (up to 700 m) that reflect tectonic influences linked with continental rifting. These formations are emplaced in an alluvial to deltaic environment evolving in a shelf depositional setting with storm and tidal effects protected by barriers (Durand and Noblet, 1986; Guillocheau and Rolet, 1982; Suire et al., 1991).

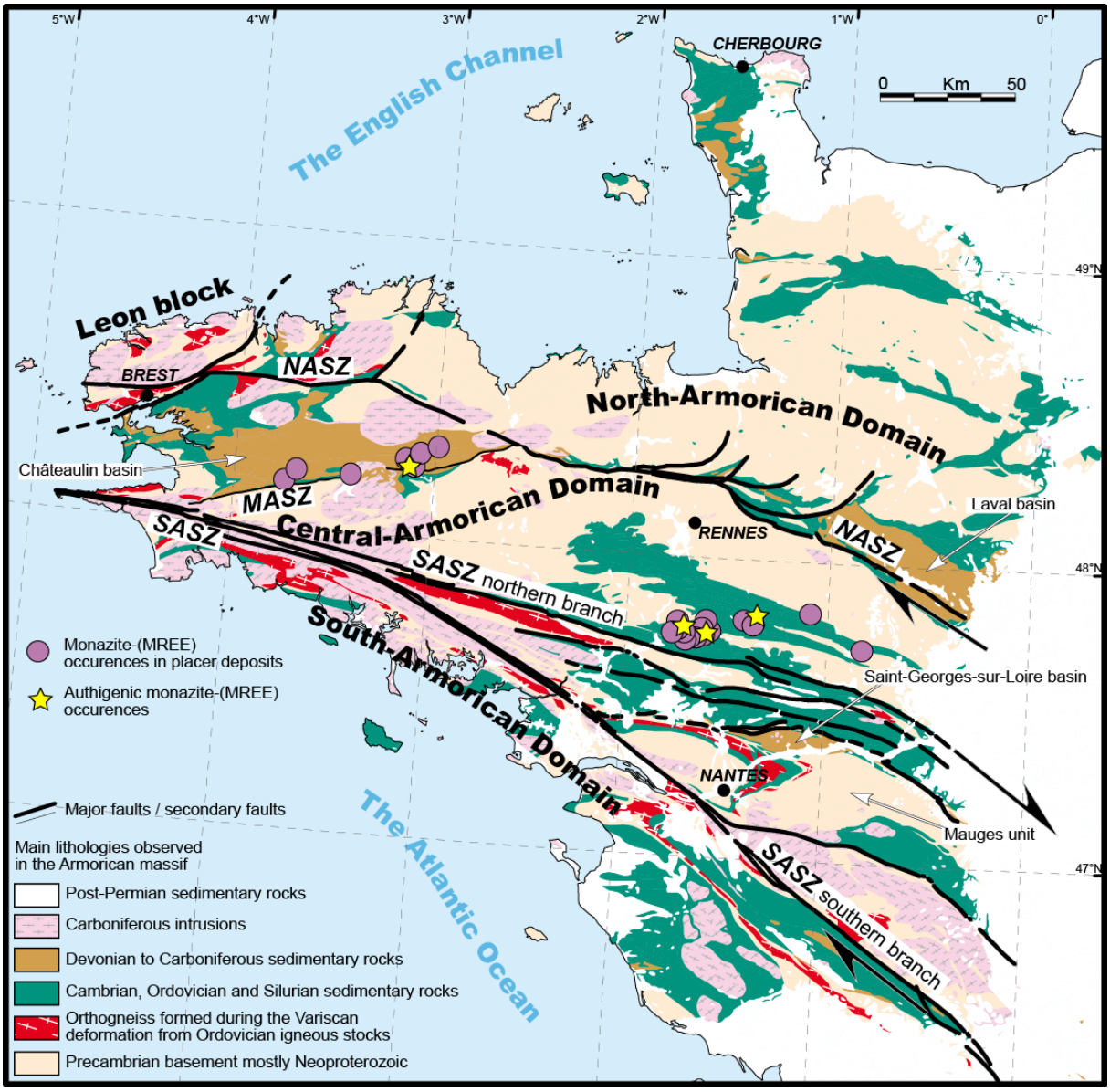

Fig. 1: Simplified map of the main structural domains of the Armorican Massif showing the distribution of authigenic monazite-(MREE) occurrences and those in placers (Geology modified from Chantraine et al., 1996; monazites occurrences from Guigues and Devisme, 1969). NASZ: North Armorican Shear Zone; SASZ: South Armorican Shear Zone

During the Middle Ordovician (Dapingian and Darriwilian) and up to the Sandbian (base of the Upper Ordovician), the sedimentation is represented by the overlying silty–clayey formations (400-500 m) that may also host sandstones and (or) phosphate nodules (Dabard and Loi, 2012). The Middle Ordovician Angers-Traveusot (MOAT) formation deposited in a storm-dominated shelf environment controlled by more uniform subsidence patterns and suggesting a post-rift setting (Dabard et al., 2007).

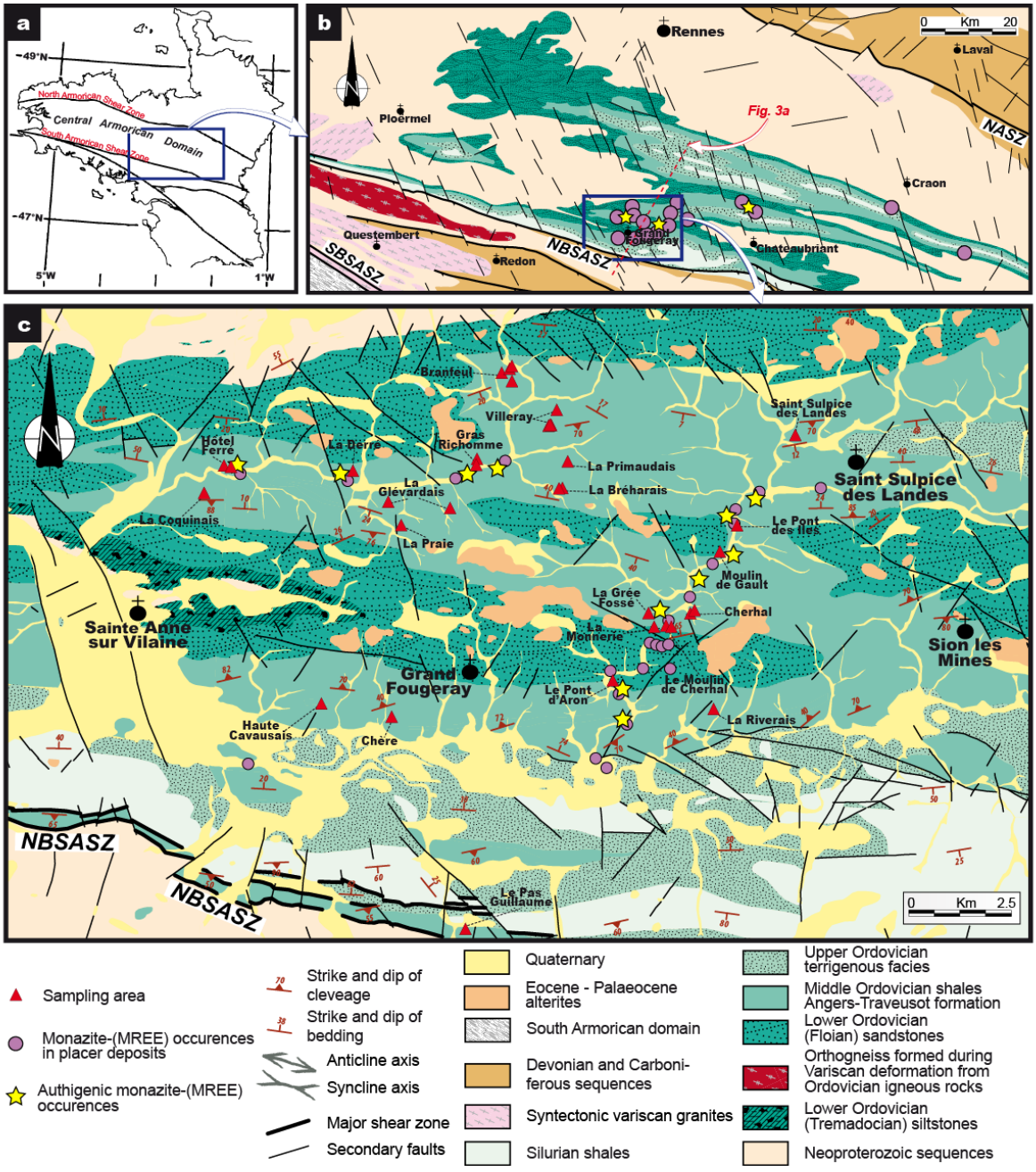

Fig. 2: a) Sketch of the Armorican Massif. b) Regional geological map of the eastern Central Armorican domain showing the main geological entities and the studied area (modified after Chantraine et al., 1996). C) Geological map of the study area modified from Dadet et al. (1987 and 1995) and Trautmann et al. (1984 and 1987). The Palaeozoic sedimentary formations are folded at long wavelenght by N110°E-trending upright folds. The succession of synclines and anticlines is controlled by the thick and competent Grés Armoricain formation dated as Lower Ordovician. The monazite-rich layers were sampled in the Angers-Traveusot formation (Middle Ordovician shales). The map uses a Lambert Conformal Conic Projection for France (RGF 1993 Zone 7). NASZ: North Armorican Shear Zone; NBSASZ: North Branch of the South Armorican Shear Zone; SASZ: South Armorican Shear Zone.

The geographic distribution of these Middle (Dapingian, Darriwilian) to Upper Ordovician (Sandbian) shelf deposits and associated faunas indicates a southward depth gradient, from near-shore environments toward more distal and deeper environments which correspond to the study area (Henry, 1989; Robardet et al., 1994). After a major sea-level fall, the sedimentation continued during the Upper Ordovician with the Katian terrigenous facies and the Hirnantian glaciomarine facies (Dabard et al., 2015; Robardet and Doré, 1988). Although stratigraphic gap has been highlighted during the early Silurian (Llandovery), marine conditions of sedimentation prevailed up to the base of the Lower Devonian (Lochkovian) giving organic-rich shales. From Pragian to Emsian (Lower Devonian), sedimentary deposits are made up of silico-clastic facies with some carbonated reefs intercalations. Wrenching along the crustal shear zones bordering the CAD (*i.e.* the NASZ and SASZ), induced the location of Middle Devonian to upper Carboniferous terrigenous and marine depocentres within individualised longitudinal basins (*e.g.* Laval and Chateaulin basins).

Squeezed between these two major structures, the CAD underwent a regional pervasive N120–125-striking dextral deformation that produced upright folds with E–W sub-horizontal axes and sub-vertical axial planes during the Variscan orogeny (Gapais and Le Corre, 1980; Gumiaux et al., 2004). From macro- to microscopic scale, the CAD is affected by important vertical fracturing (strike-slip faults and extensional fractures) with a dominant N160°E orientation oblique to fold axes (Fig. 4a). Choukroune et al. (1983) demonstrated that this fracturing was compatible and coeval with the CAD-scale Carboniferous dextral strike-slip that occurred via successive incremental deformation during clockwise rotation of principal strain axes. Although the CAD appears as a zone of relatively weak deformation, and the strain intensity increases on moving north and south, *i.e.* towards the NASZ and the SASZ. In the studied area, this regional strain gradient is assumed to be associated with an increase of metamorphic conditions towards the south, *i.e.* both the northern branch of the SASZ (NBSASZ) and the southern branch (SBSASZ), with local pertubations due to variscan granite emplacement (Le Corre, 1975; Le Corre and Le Theoff, 1976). As a consequence, Tartèse et

al. (2015) demonstrated using in-situ U-Pb geochronology on both xenotime and monazite that successive hydrothermal events over about 90 Ma, from *ca.* 420 to 330 Ma occurred in the CAD. A time interval that encompasses most phases of the construction of the Variscan orogeny in Brittany.

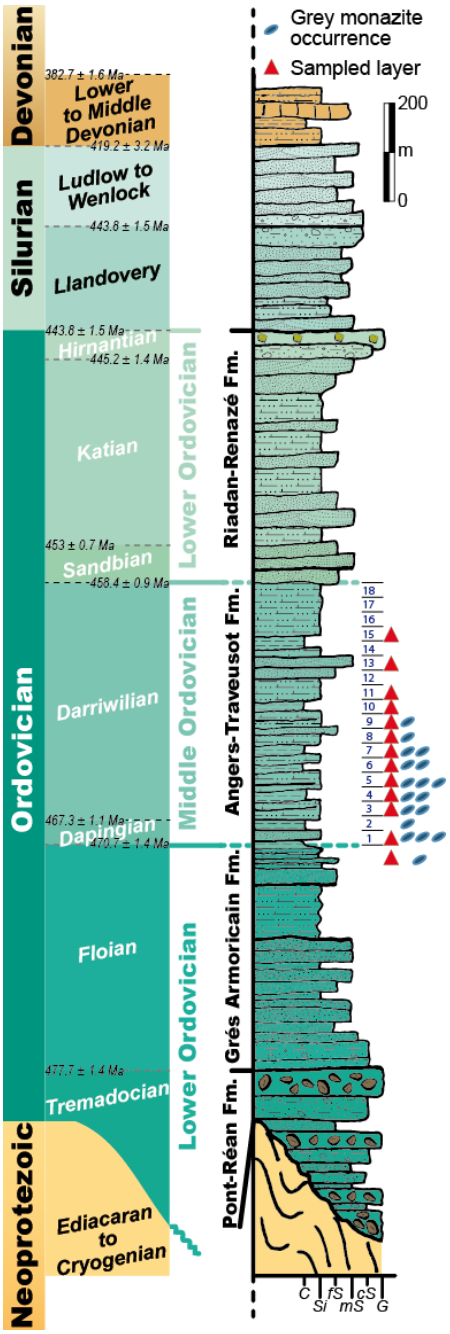

Fig. 3: Lithologic column of the lower Palaeozoic formations observed in the studied area (from Dadet et al. (1987 and 1995) and Trautmann et al. (1984 and 1987)). Locations of monazite-rich levels and distribution of stratigraphic sequences modelled into 18 levels using the potential-field interpolation method (see below). C: claystone, Si: siltstone, fS: fine sandstone, mS: medium sandstone, cS: coarse sandstone, G: granule; Fm. Formation.

Although several NGM placer deposits have been discovered in the whole Armorican Massif related to pre-Pennsylvanian sequences (Guigues and Devismes, 1969), only the eastern CAD in the south of Rennes provides both numerous placers and authigenic deposits at the same location (Figs. 1 and 2). These NGM occurrences have been discovered in the MOAT formation close to Grand-Fougeray by BRGM exploration works (Donnot et al., 1973; Guigues and Devismes, 1969; Guigues and Sapinart, 1967). They are related to low metamorphosed black-shales (also named Angers-Traveusot Formation or Postolonnec Formation) which are characterized by small size grains of quartz, sericite, illite, kaolinite, chlorite and chloritoid that have been described in addition to graphite, pyrite and iron oxides (Donnot et al., 1973). Ilmenite and rutile also occur. Monazite is represented by

microcrystalline grey nodules (0.1 – 2.0 mm in size) disseminated in different proportions within shales (50 – 200 g/t). Monazite nodules have been subsequently concentrated in proximal alluvial placers by weathering processes. Within the Ordovician stratigraphy (Figs. 2 and 3), the NGM bearing shales (Middle Ordovician) overlie oolithic iron formations and sandstones (Grès Armoricain from the Lower Ordovician) that are enriched in detrital rutile, ilmenite, zircon and rare monazite (Donnot et al., 1973; Gloaguen et al., 2007; Moëlo et al., 2008). Also note that the silty-clayey beds of the UPLO formation at Le Pont d'Aron also host NGM. Donnot et al. (1973) proposed that early diagenesis was of prime importance in the grey monazite forming processes suggesting the following evolution: (**i**) precipitation of amorphous REE phosphate in marine silts; (**ii**) crystallisation into fibrous nodules of rhabdophane; (**iii**) replacement of rhabdophane into grey monazite-(MREE).

2. Material and methods

2.1. Sampling

Although the studied area belongs to lowland farm fields and the outcrop conditions are very poor, small abandoned quarries allowed us to define a sampling strategy. The objective is to evaluate the distribution of NGM grains in the whole MOAT formation and the relationships with metamorphism and deformation gradient. Samples from the MOAT formation were therefore collected on 36 outcrops (Fig. 2). Note that three outcrops from the UPLO formation have been sampled as well (Fig. 3). They comes from Le Pont d'Aron and La Monnerie area (Figs 2 and 3). Heavy NGM concentrates were also sampled in La Monnerie placer deposit that correspond to former BRGM works in the 1960's.

2.2. 3D modelling of the MOAT formation folding

The pattern of repeated bedding of the MOAT formation that corresponds to the intersection between geological 3D plunging fold features with the surface topography has been divided into stratigraphic sequences (n = 18) according to the potential-field interpolation method implemented in the 3D GeoModeller software (see Calcagno et al. 2008 for method).

2.3. X-ray diffraction analysis and Kübler index

Major mineral assemblages (quartz, feldspars, oxides and sheet silicates) are characterized optically on thin section under the microscope and by X-ray diffraction analyses. Thin sections of all the samples were studied under the optical microscope. XRD analyses were realised for representative rocks. X-ray diffraction analysis was performed using a D8-Advance Bruker-AXS (Siemens) diffractometer, Ni-filtered CuKα radiation at 40 kV and 40 mA and primary soller slit of 2.5° and divergence slit of 0.6 mm; secondary soller slit of 2.5°, with detector slit of 0.1 mm and antiscattering slit of 0.6mm. Samples were crushed using an agate mortar pestle mill. Analyses of the relative content of minerals were performed with a step length of 0.02° and a scan speed of 1.2°/min over the range 2°–70°2θ for whole rocks composition. For air-dried, ethylene glycol solvated and heated samples, measurements were performed with a step length of 0.02° and a scan speed of 0.6°/min over the range 2°–35°2θ. More specifically for the sheet silicate determination, powder samples; air-dried, ethylene-glycolated and to 550 °C heated textured samples were used to precisely characterize the different micas as muscovite and clay minerals. Mineral quantification was performed on whole-rock powder specimen, using the software DIFFRACPlus EVAL v 12.0 (©Bruker AXS). This method is based on the determination of the peak intensity in counts per second of the ten most representative peaks of the specific mineral.

Twenty-one samples of MOAT formation (Grand Fougeray area) and eight samples of UPLO silty-clayey formation (Le Pont d'Aron area) (Figs. 2b, 3 and 5) have been selected to calculate their Kübler-Index (KI) and Árkai-Index (ÁI) from the FWHM of illite/muscovite and chlorite on the air-dry powder diagram respectively. The Kübler-Index (KI; Guggenheim et al., 2002), also termed ''illite crystallinity'' in earlier literature (Frey, 1987), is a well-established method for characterising the metamorphic grade of pelites in very low-grade metamorphic environments. The method measures the full width at half maximum intensity (FWHM) of the first illite basal reflection in XRD patterns and expressed in Δ°2θ (Frey, 1987; Guggenheim et al., 2002). The KI is mainly controlled by the thickness of illite/muscovite crystallites (e.g. Merriman and Peacor, 1999; Merriman et al., 1990; Merriman et al., 1995) and is also influenced by the lattice strain and other lattice imperfections (Merriman and Peacor, 1999). For the KI study, clay mineral separation was conducted using techniques described by Schmidt et al. (1997) and following the recommendations of Kisch (1991). KI herein used to define the limits of diagenesis to metamorphic zones, following the recommendations for Kübler-Index calibration of Ferreiro Mählmann and Frey (2012) and the CIS-KI transformation formalism of Warr and Ferreiro Mählmann (2015). The zone boundary values are the following: KI ≤ 0.25 Δ°2θ for the epizone, the upper anchizone boundary 0.25

≤ KI ≤ 0.33 Δ°2θ, the lower anchizone boundary and 0.33 ≤ KI ≤ 0.42 Δ°2θ, and the diagenetic zone when KI ≥ 0.42 Δ°2θ. A lower and upper diagenetic zone is defined at KI = 1 Δ°2θ. The same experimental conditions were used to determine chlorite "crystallinity" on the 7 Å (002) peak of chlorite, where (ChC(002)) corresponds to the FWHM value of the second (7 Å) basal reflection. The ChC(002) measurements were also standardized with the CIS sample-set of Warr and Rice (1994) and expressed as the Árkai index (ÁI) according to the formulism proposed by Guggenheim et al. (2002): ÁI=1.621 ∗ ChC(002)+0.006. Data are reported in the Supplementary Appendix 1.

2.4. Whole rock analyses

Whole-rock chemical analyses of shales were performed on crushed and pulverized rock samples at Acme Analytical Laboratories (Vancouver, Canada). Major oxides and trace elements were determined using ICP-MS. Loss on ignition (LOI) was calculated by weight difference after ignition at 1000°C. Total abundances of the major oxides and several minor elements are reported on a 0.2 g sample analysed by ICP Emission Spectrometry following a lithium metaborate/tetraborate fusion and dilute nitric digestion. Rare earth and refractory elements are determined by ICP Mass Spectrometry (ICP-MS) following a lithium metaborate/tetraborate fusion and dilute nitric digestion of a 0.2 g sample. Total carbon was determined using LECO. Data are reported in the Supplementary Appendix 2.

2.5. Analysis of carbonaceous materials

Rock Eval 6 pyrolysis (Vinci Technologies®) was performed ISTO laboratory (CNRS / University of Orléans, France) under standard conditions with a linear increase temperature program of 30°C.min^{-1} (Lafargue et al., 1998). The final temperature reaches 650°C in the pyrolysis oven and 750°C in the oxidation oven. This analysis provides the following parameters: TOC (expressed in %), Tmax (expressed in °C), HI (expressed in mg HC/g TOC), OI (expressed in mg CO_2/g TOC) and S2 (expressed in mg HC/g rock). Data are reported in the Supplementary Appendix 3.

2.6. Scanning Electron Microscopy, Cathodoluminescence & Electron Probe MicroAnalysis

Monazite grains were studied in detail at the ISTO-BRGM laboratory in Orléans using a Tescan Mira 3 XMU (Tescan, Brno, Czech Republic) scanning electron microscope (SEM) along with optical reflected

and transmitted light imaging. The SEM is coupled to a back-scattered electron (BSE) and a panchromatic cathodoluminescence (CL) detector (350–650 nm, TESCAN BSE/CL detector) and produces images in order to assess compositional variations and textures. Additional SEM-EDX information about mineral inclusions was determined as well. Monazite and xenotime compositions were determined with Cameca SX50 electron probe micro-analyser (EPMA) at the ISTO-BRGM laboratory in Orléans, equipped, with five wavelength dispersive spectrometers using the following standards, X-ray lines and analysing crystals: Ca (natural apatite, Kα, PET), P (synthetic $NdPO_4$, Kα, TAP), Si (natural albite, Kα, TAP), Fe (synthetic Fe_2O_3, Kα, LIF), La (synthetic $LaPO_4$, Lα, PET), Ce (synthetic $CePO_4$, Lα, PET), Pr (synthetic $PrPO_4$ Lβ, LIF), Nd (synthetic $NdPO_4$, Lα, LIF), Sm (synthetic $SmPO_4$, Lα, LIF), Eu (synthetic $EuPO_4$, Lα, LIF), Gd (synthetic $GdPO_4$, Lβ, LIF), Y (synthetic YPO_4, Lα, TAP) and Th (synthetic ThO_2, Mα, PET). An accelerating voltage of 20 kV with a beam current of 100 nA and a beam diameter of about 1-2 µm, were used to analyse minerals. Counting times on peaks were twice that of background, with 40 s for each element. Over 440 analyses have been performed. Detection limits are the following: 0.1 g/kg for Ca, P and Si; 0.2 g/kg for Fe; 0.3 g/kg for Y; 0.4 g/kg for La and Ce; 0.5 g/kg for Nd; 0.6 g/kg for Sm, Th; 0.8 g/kg for Pr; 0.9 g/kg for Eu and Gd. For all the chemical compositions, only the significant values with an accuracy of 95% [(peak-background) × counting time > 2 × √ (background × counting time)] were retained. Results are reported in the Supplementary Appendix 4.

2.7. U/Pb geochronology

Two different analytical protocols were subsequently implemented for both heavy NGM grains from La Monnerie placer deposit and monazite types observed in thin sections. **i**) Heavy monazite grains from concentrate were hand-picked under a binocular microscope. Grains were mounted in epoxy resin and subsequently ground and polished until the crystal centres of the grains were exposed and to obtain a flat surface. Grains were imaged using SEM BSE-CL. Dating were performed at the BRGM laboratory (Orléans, France). Polished sections were analysed using an ICP-MS Xserie II (Thermofisher) configured to Xs cone, coupled to a laser Cetac Excite 193nm. Samples were located in Two volum HelEx II® ablation chamber and ablated material are transported by He flux and mixed to Ar and N2 before entering the plasma. **ii**) Monazite grains from different paragenesis were also located in polished thin sections, imaged using SEM BSE-CL than analysed. Dating were performed at the ISTO laboratory (CNRS / University of Orléans, France). Monazite grains were analysed using an ICP-MS 8900 (Agilent)

configured coupled to a laser asi® RESOLution Excite 193nm. Samples were located in two-volume chamber and ablated material are transported by He flux and mixed to Ar and N_2 before entering the plasma. Conditions of ablations and analyses are summarised in the Supplementary Appendix 5.

Analyses are standardised with respect to the monazite of Trebilcock (272 ± 2 Ma, Tomascak et al., 1996), and quality control was performed via two standards: the Madmon (515 Ma, Schulz et al., 2007) and Namaqualand (1033 Ma, Knoper et al., 2000). Data reduction was carried out with Glitter® software and no common lead correction was applied. The results are generated using IsoplotR by Vermeesch (2018) at 95% of confidence by taking errors at 2σ. The correlation factor rho was calculated according to the simplified equation of Schmitz and Shoene (2007). Results are reported in the Supplementary Appendix 6.

3. Results

3.1. Field constraints

In the eastern CAD, south of Rennes (Fig. 2), Palaeozoic sedimentary rocks are mainly exposed in small relatively well preserved quarries. The investigated MOAT formation is mostly composed of black-shales (Fig. 3) that may be oxidised and contains numerous siliceous nodules and fossils of graptolites, conodonts and trilobites. Consistent with the literature (Ballèvre et al., 2009; Gapais and Le Corre, 1980; Gumiaux et al., 2004; Jégouzo, 1980; Le Corre et al., 1991; Le Corre and Le Theoff, 1976), strata show a constant ESE strike with a broad low dip toward both the north (22°) and south (17°) suggesting an upright fold system with ca. N110°E-trending fold axis (Fig 4a, b, c). Locally, the strikes and (or) dip directions may be disturbed because of asymmetric plunging fold geometry (the north-directed limb may be moderately inclined: ca. 30-50°), periclinal endings, or tilted along NW-SE vertical faults (Figs. 2b, 4b). Folds are associated with an axial-plane slaty cleavage that is roughly vertical and strikes E-W to N110°E (Fig. 4d). Cleavage's strikes may also show local deflections along NW-SE-trending faults (Fig. 4d). A discrete sub-horizontal stretching lineation has been observed even though it is more easily observable south of the Grand Fougeray town, in the vicinity of the NBSASZ suggesting the deformation increases southward reaching a maximum along the SASZ (Fig. 1).

3.2. Rock forming minerals

3.2.1. Mineral characterisation, Kübler and Árkai-Indexes

The black shales samples appear mostly monotonous, although sometimes disturbed by silty lenses or beds. The rocks are made up of various modal proportions of quartz (from 26 to 65 %, with means - □ - and standard deviations at 46 % ± 11), sometimes feldspar mostly plagioclase (3 to 39 %, □ = 11.4 % ± 11), in a clay mineral matrix (13 to 69 %, □ 42.5 % ± 12) consisting in a very fine-grained mixture of kaolinite, interstratified illite/smectite, chlorite (chamosite-clinochlore and rare corrensite) and sericite. According to the potential-field interpolation method, the illite/smectite ratio is higher in the lower part of the MOAT formation.

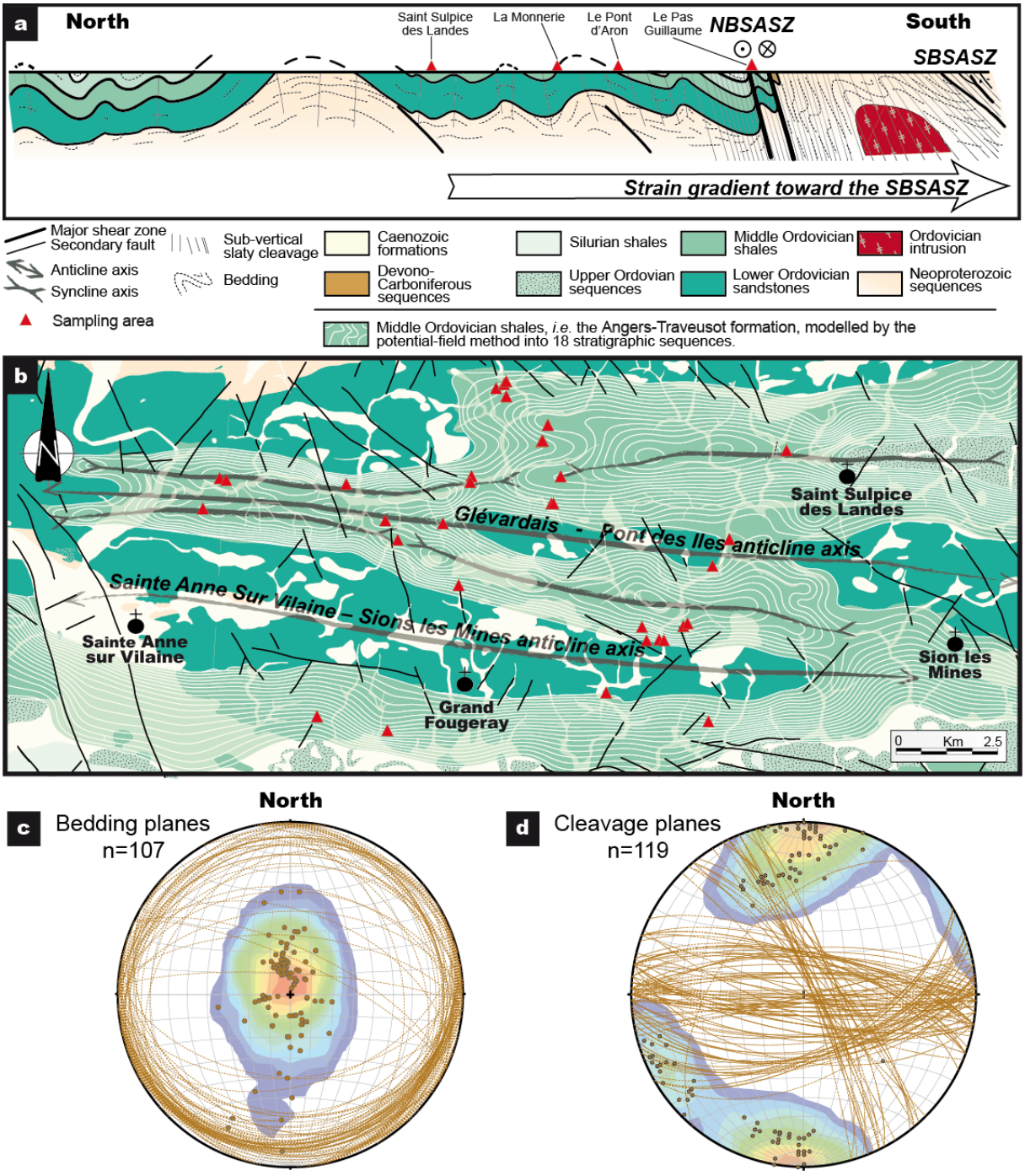

Fig. 4: a) A simplified cross-section of the eastern part of the Central Armoricain domain. The Northern Branch of the North-Armorican shear zones cut across a pile of rocks that undergo North-South increasing deformation gradient. b) Simplified geological map of the Grand Fougeray area. Main fold axes are highlighted such as the Sainte Anne sur Vilaine – Sions les Mines anticline axis. The Anger-Traveusot formation has been subdivided into 18 stratigraphic sequences using the potential-field interpolation method. Stereographic projection (Schmidt's lower hemisphere equal-area projection) of

(c) bedding planes of Palaeozoic sedimentary rocks and (d) cleavage planes. Planes are represented by their respective poles and density plots.

Note there is no clear correlation in the distribution and modal proportions of chlorite with respect to the strain gradient, and that sericite may be detrital flakes of $2M_1$ muscovite or an authigenic illite/muscovite assemblage. Biotite is scarce although most frequent in the UPLO silty-clayey formation of Le Pont d'Aron. Opaque minerals (pyrite, iron oxides), apatite, rutile, titanite and zircon, with grey monazite are common accessories. Note that pyrite is frequently oxidised and replaced by iron oxides.

The KI values determined in the MOAT black shales and UPLO silty-clayey range from 0.80 to 0.25 Δ°2θ corresponding to metamorphic grades evolving from the diagenetic toward the transition between the anchizone and epizone domains respectively from the bottom to the top of the stratigraphic sequence (Fig. 5a; Appendix 1). The correlation between the KI and ÁI shows some outliers (Fig. 5b), mostly in the anchizone domain, which are attributed to possible interferences with chloritised biotite, and(or) differences in successive chlorite crystallisation with different compositions (*i.e.* clinoclore *vs.* chamosite). When excluding outlier data, correlation is rather good (R^2 = 0.68, Pearson's r = 0.83), with concomitant evolution of both index with increasing metamorphism (Fig. 5b).

Considering the distribution of metamorphic grades (Fig. 5a), KI values tend to decrease from the upper part of the MOAT to the Lower – Middle Ordovician limit where high-grade anchizonal and probable epizonal metamorphic conditions are reached in Le Pont d'Aron area. Indeed, very low-grade metamorphic conditions with the highest KI values (diagenesis) are mostly located in the upper two-third part of the MOAT formation, whereas lower anchizonal conditions preferentially occur in the lower third part of the MOAT formation. One can note that KI values from Saint Sulpice des Landes may appear low with respect to its position in the upper part of the stratigraphic sequence. This can be the result of local geological features (*e.g.* unreported faults with fluid circulations that altered the rocks) or analytical bias. One may also consider an analytical bias for La Praie where KI value appears exceptionally high therein.

This result consistent with Le Corre (1975) help us to infer the distribution of the upper anchizonal and epizonal domains in the Lower Ordovician sequences and older units (Fig. 5c). The potential-field interpolation method integrating the KI values stresses the upright folds with E–W sub-horizontal axes units and suggests an increase of metamorphic grades along the stratigraphic sequences (Fig. 5c). There is no relation between the metamorphic conditions and the position to the NBSASZ.

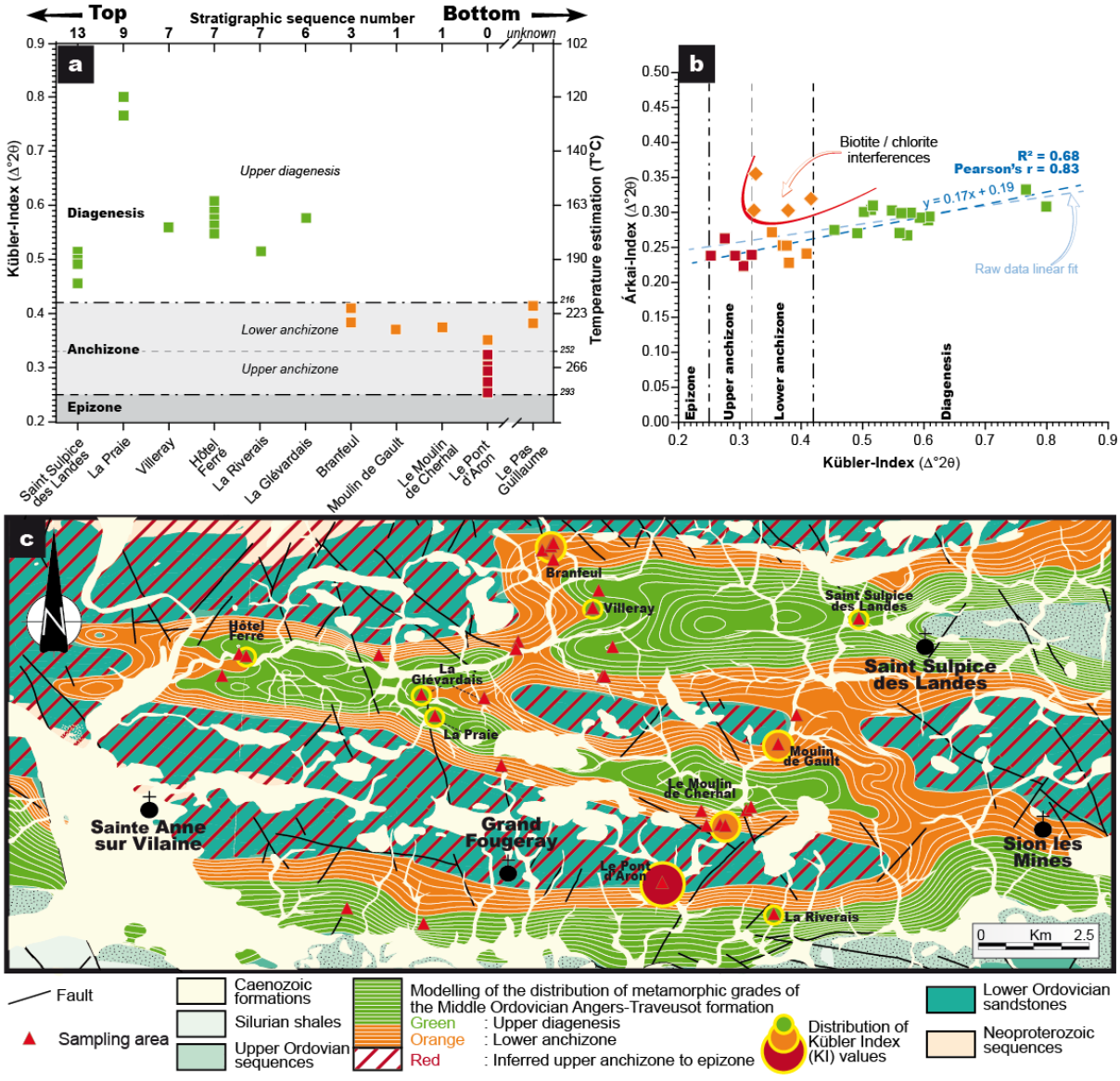

Fig. 5: a) Distribution pattern of Kübler Index (KI) of samples from Middle Ordovician shales in the Grand Fougeray area function of their location in the modelled stratigraphic sequences. (b) Correlation between KI (10 Å) and ÁI (7 Å) values. Data with probable biotite interferences have been excluded of

the reported correlation coefficient. c) Distribution of metamorphic grades according to KI values on the simplified geological map of the Grand Fougeray area. The diagenetic and lower anchizonal domain are modelled within the MOAT formation according to the potential-field interpolation method. Location of the upper anchizonal and epizonal domains in the Lower Ordovician sequences and older units is inferred according to data observed in Le Pont d'Aron area and Le Corre (1975) works. Metamorphic zone boundaries for KI values are after Warr and Ferreiro Mählmann (2015). Palaeotemperature reconstruction from KI are from Zhu et al. (2016).

3.3. Geochemical features of the MOAT formation

Whole rock geochemistry of black shales (Appendix 2) from 35 localities (Fig. 2b) shows a relatively uniform chemical composition in both major and trace elements. According to the distribution pattern of the Kübler Index (KI) with respect to the potential-field interpolation method, we adopt below the following graphic chart and consider in red, samples belonging to the upper anchizone/epizone domain (UPLO formation) and in orange and green, samples belonging to the lower anchizone and diagenetic domains of the MOAT formation respectively.

3.3.1. Inter-element relationships: using major elements data

Contents in SiO_2 and Al_2O_3 show gathered and uniform patterns (Fig. 6a, from 421 to 683 g/kg, □ = 516 g/kg ± 46, and from 130 to 283 g/kg, □ = 241 g/kg ± 24, respectively) with respect to upper continental crust composition (UCC; McLennan, 2001). Also note that Al_2O_3 and SiO_2 are negatively correlated. Hence, the considerable increase in SiO_2 content of the MOAT formation highlight a lithological heterogeneity and beds enriched in quartz. The FeO_T content (from 29 to 188 g/kg, □ = 86 g/kg ± 2.6) is, on average, slightly enriched with respect to UCC, especially when considering samples from the diagenetic domain (*i.e.* the upper part of the MOAT formation). By contrast, the CaO content (from 0 to 18 g/kg, □ = 2.3 g/kg ± 3) is very low and all patterns show a moderately to strongly depleted anomaly. Actually, samples belonging to the anchizonal domain (*i.e.* the lower part of the MOAT formation) appear, on average, the most depleted in CaO, MgO and also Na_2O, but they are enriched in K_2O (Fig.

6a). Conversely, the P_2O_5 content is variable and displays both positive and negative anomalies. Indeed, if the diagenetic samples are pretty similar with UCC references, samples from lower anchizone domain are depleted, whereas samples from the upper anchizone are enriched in P (Fig. 6a).

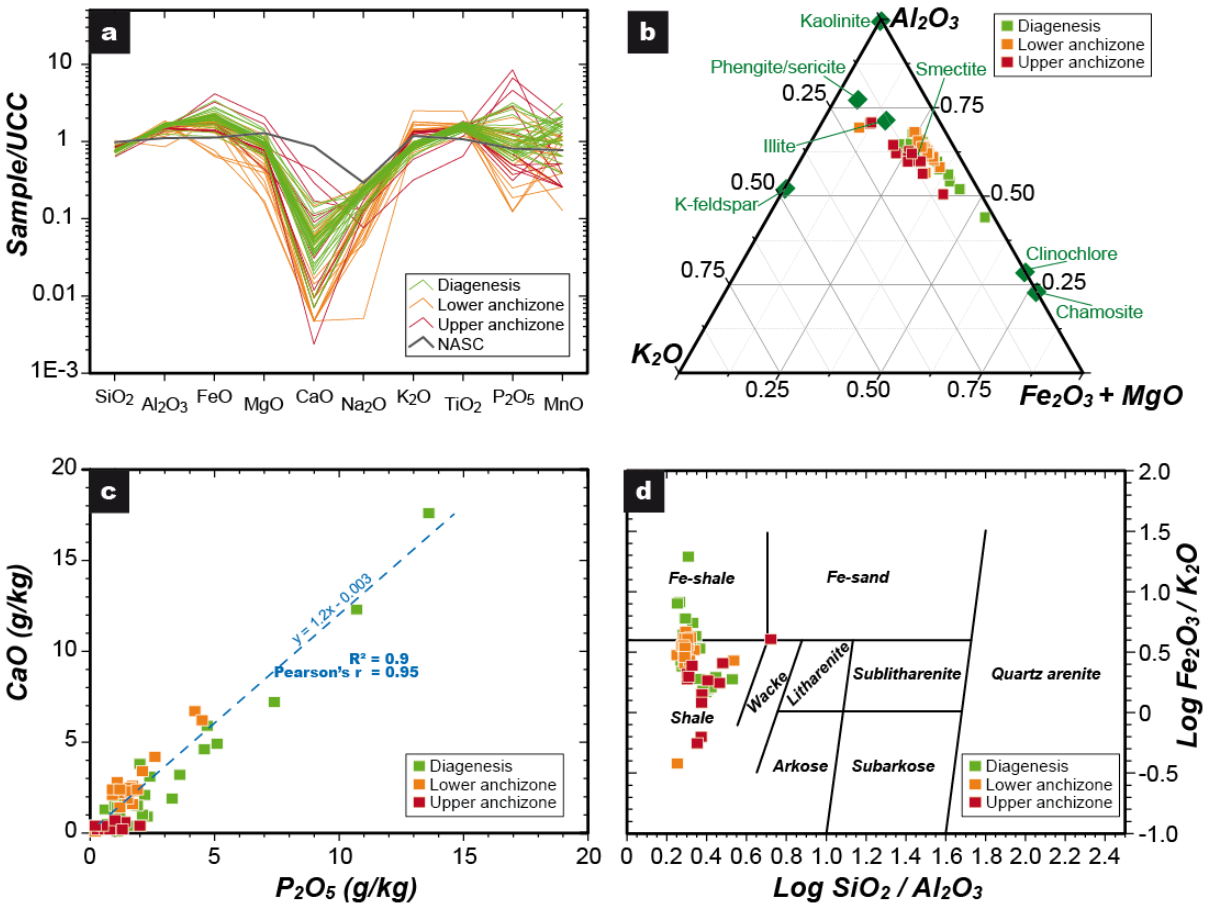

Fig. 6: a) Major element enrichment of Middle Ordovician shales from the Grand Fougeray area normalized to Upper continental crust (UCC). b) $Al_2O_3/K_2O/(Fe_2O_3+MgO)$ ternary diagram for the whole analysed shales belonging to the MOAT. c) CaO versus P_2O_5 element distribution. Because samples belonging to the upper anchizone do not correlate well with the other domains, they have been discarded for the correlation coefficient calculation. d) Log SiO_2/Al_2O_3 versus log Fe_2O_3/K_2O geochemical classification plots for sedimentary rocks from Herron (1988). Data are presented with respect to their provenance in the Lower and Middle Ordovician formations (diagenesis, lower and upper anchizonal domains, according to Fig. 5b).

Variations in Al_2O_3, K_2O and Na_2O may highlight the occurrences of feldspar when SiO_2 is high (silty layers), or phyllite (illite, chlorite and detrital muscovite). In the Al_2O_3, K_2O and Fe_2O_3+MgO ternary diagram (Fig. 6b), data plot between the chlorite – phengite/sericite endmembers, thus suggesting that the rock-forming minerals are controlled by aluminous phases mainly represented by illite–smectite and chlorite. In the MOAT formation, both P_2O_5 and CaO show a very high correlation (R^2 = 0.9, Pearson's r = 0.95, Fig. 6c), and with a CaO/P_2O_5 ratio of about 1.2. It may imply a mineral association in the form of apatite ($Ca_5(PO_4)_3(OH, F, Cl)$ with CaO/P_2O_5 about 1.3. Note that in the upper anchizone domain, *i.e.* rocks belonging to the underlying UPLO silty-clayey formation, this assumption is not true as CaO is very weak. This therefore precludes the occurrence of carbonate such as calcite in both units. After all, the geochemical classification of terrigenous sandstones and shales (Herron, 1988), and according that most samples display $0.2< Log(SiO_2/Al_2O_3) <0.6$ and $-0.4< Log(Fe_2O_3/Al_2O_3) <1.3$, the studied samples consist of shales and Fe-shales (Fig 6d). Iron-shales are mostly observed in the upper part of the MOAT formation (*i.e.* the diagenetic domain, Fig 5). Wackes remain scarce (1 sample) and belong to La Monnerie area, *i.e.* the UPLO formation.

3.3.2. Inter-element relationships: using trace elements data

In siliciclastic sediments like sedimentary rocks, K distributes mainly in K-feldspar, mica and clay minerals both of detrital and diagenetic origins. The distribution of Rb, as well as K, in grain-size fractions depends on sediment maturity. Indeed, both elements are equally distributed for all grain sizes in immature sediments, whereas in mature sediments, they are carried by clay minerals in the finest fraction (Matys Grygar et al., 2019; van de Kamp, 2016; von Eynatten et al., 2016). Thus the plot of K/Rb against K/Al (Fig. 7a), shows a field for modern sediments (muds) that occurs in the range of K/Rb < 220 and K/Al < 0.25. In the course of buried and diagenesis, such sediments will become shales then altered shales and will undergo in an open-system, progressive mineralogical modification including the phyllic paragenesis evolving from Al-rich phase such as kaolinite and smectite, to K-enriched phases

such as illite, muscovite/biotite and K-feldspars. Such sediments may also undergo hydrothermal alteration. By analysing the K/Rb ratio, it is possible to use both K and Rb as proxies for metasomatic processes during diagenesis (van de Kamp, 2016). The K/Rb versus K/Al plot for both the MOAT and the underlying UPLO silty-clayey formations of the Grand Fougeray area, shows a nice trend with high positive correlations ($R^2 = 0.84$ and Pearson's $r = 0.92$) suggesting a slight K enrichment (Fig. 7a). In details, most samples belonging to the diagenetic and lower anchizone domains plot within the limit of Holocene and Pleistocene muds, i.e. shale that not have been altered or underwent very minor modifications (Fig. 7a). This may suggest that rocks have been preserved and have evolved under the effects of isochemical-like diagenetic processes. In only the following few locations, rock sample composition evolves and falls beyond that limit (Fig. 7a). It concerns all the samples belonging to the UPLO formation (upper anchizone domain), and a few localities belonging to the lower anchizone domain (Le Moulin de Cherhal), the diagenesis domain (all the samples from Saint Sulpice des Landes) and a locality where both the diagenetic and lower anchizonal conditions have been observed (La Glévardais). In that cases, sedimentary rocks may have been altered and undergone K-metasomatism in an open system.

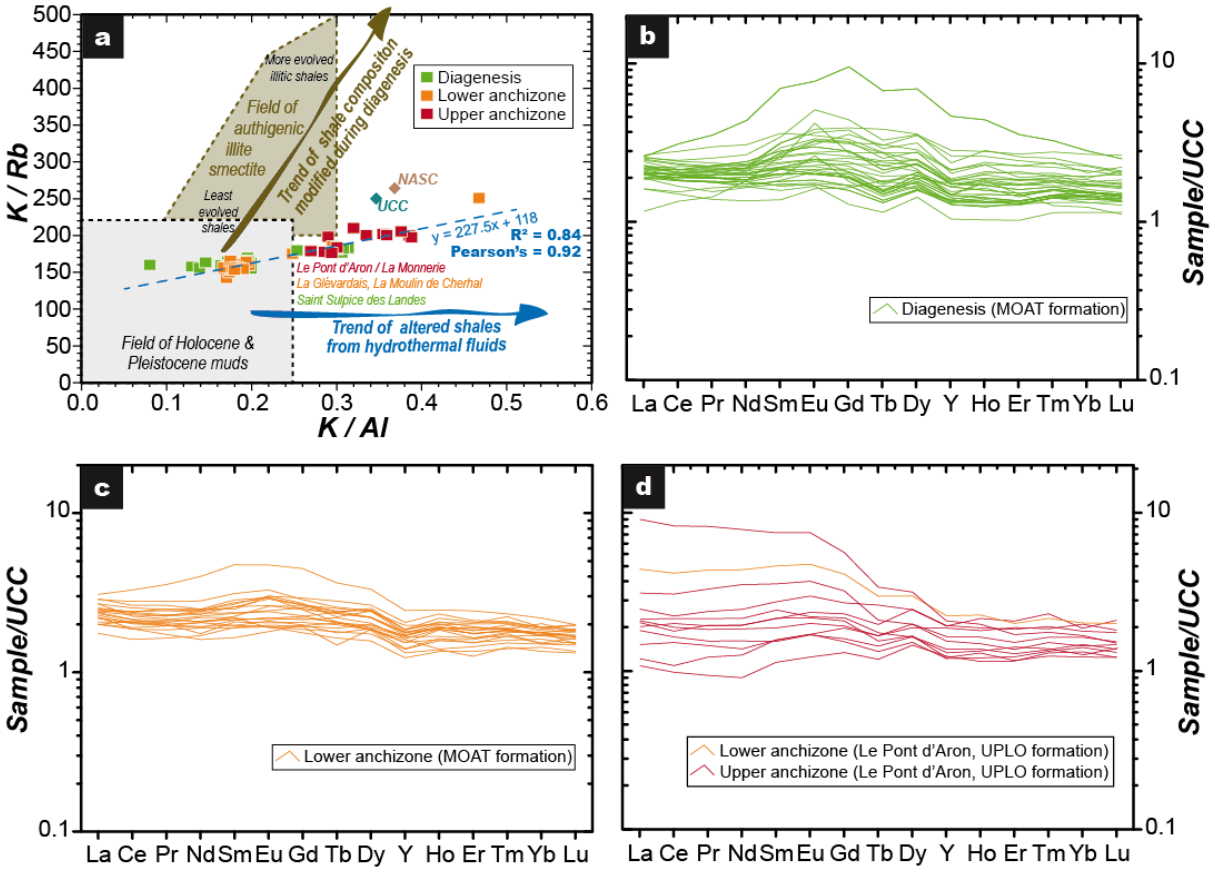

Fig. 7: a) K/Rb versus K/Al for muds and shale from van de Kamp, (2016). Most detrital clays plot within the range of 0.0< K/Al <0.25 and 0< K/Rb <220. Diagenetically modified shales with added K and Rb commonly fall outside these limits in a distinct field. UCC-normalised REE patterns in samples from b) the diagenetic domain c) the lower anchizonal domain, and d) the upper anchizonal domain. UCC values are from McLennan (2001). Data are presented with respect to their provenance in the MOAT and UPLO formations (diagenesis, lower and upper anchizonal domains, according to Fig. 5b).

The ∑REE concentrations in shales vary from 177 to 1195 mg/kg (= 365 mg/kg ± 133) and the UCC-normalized REE patterns are differentiated. Key features concern the origin of the samples with respect to their northern or southern location. For instance, it can be observed that the REE patterns for samples from the diagenetic (Fig. 7b) and lower anchizone metamorphic grades (Fig. 7c) display a MREE enriched patterns. Besides that, samples from the diagenetic domain more frequently display this MREE enriched pattern (Fig. 7b). In details, one can observe either Eu or Sm and a Dy positive anomalies with sometimes a slight negative Ce anomaly (Figs. 7b-c). These shape bell patterns and the apex (*i.e.* Gd) may rise at one

order of magnitude above the UCC values. Concerning the upper anchizone domain, the REE patterns are slightly to highly enriched in LREE (Fig. 7d). A few patterns may be slightly enriched in MREE.

3.3.3. Inter-element relationships: the total carbon and total organic carbon characterisation

Whole rock total carbon and total organic carbon concentrations are given in Appendixes 2 and 3. Total carbon (TC) content ranges from 1.3 to 12 g/kg (= 3.7 g/kg ± 2), while total organic carbon (TOC) content range from 1 to 11 g/kg (= 4 g/kg ± 2). Both TOC and TC show a high positive correlation (R^2 = 0.93, Pearson's r = 0.97, Fig. 8a), with a slope of about 0.93. This confirms the occurrence of inorganic carbon, *e.g.* in carbonate phase, is very low and insignificant, and calculated in between 0 and 1.5 g/kg. It also highlights that most C is organic in the MOAT formation.

The ∑REE versus TC plot, reminds the pretty uniform content of shales (Fig. 8b). One can note that most samples plot along a positive slope suggesting a slight concomitant trending evolution of ∑REE with the increasing grade of organic carbon. The important dispersion observed along the y axis may be interpreted as pore fluid migration according to Rasmussen et al. (1998). Note that pore fluid migration does not tend to be a common process (Fig. 8b). Indeed, the areas for which we suggest above they have been affected by K-metasomatism (*e.g.* Le Pont d'Aron, Saint Sulpice des Landes, Fig. 7a) are preferentially affected by pore fluid migration processes.

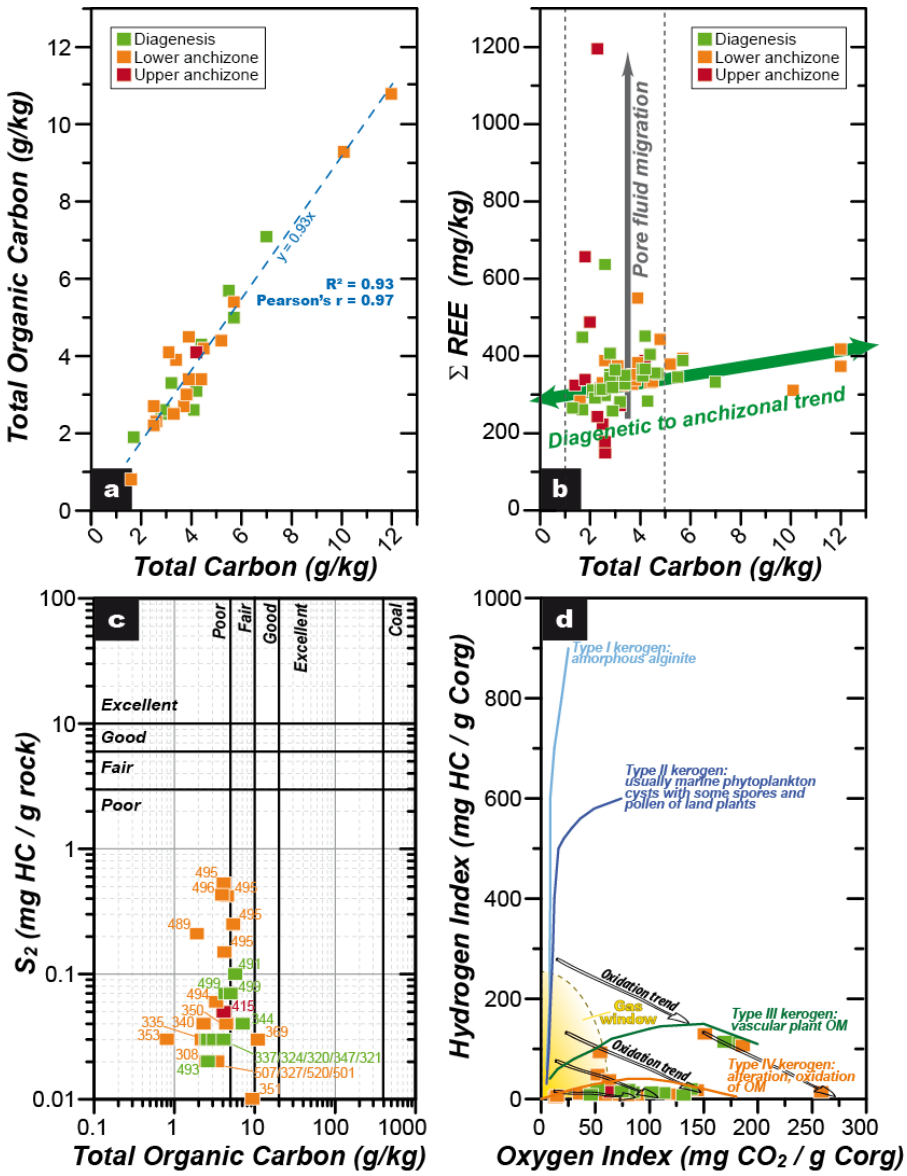

Fig. 8: a) Total Organic Carbon from Rock-Eval method (TOC) versus Total Carbon (TC). b) Distribution of samples in the ΣREE versus TC diagram. c) *Plot of the amount of hydrocarbon (HC) formed during thermal decomposition of the kerogen (S_2 value) versus TOC. The T_{max} value, a Rock-Eval maturity indicator, is shown for each sample. d) Middle Ordovician shale samples plotted on pseudo-Van Krevelen diagram. Data are presented with respect to their provenance in both the MOAT and UPLO formations (diagenesis, lower and upper anchizonal domains, according to Fig. 5b). OM : organic matter.*

With a mean of 3.7 g/kg for the TOC content, the hydrocarbon (HC) potential is assumed as poor despite some pretty fair source richness samples as shown by combining TOC and S_2 values (Fig. 8c). In detail, when the source rock matures, the amount of OM in the source rock

have to decrease with both the TOC content and the amount of reactive kerogen (Rock-Eval S2). The Tmax distribution in the S_2 versus TOC diagram, should define a general trend of maturity with highest temperatures corresponding to both low TOC and S_2 values. The absence of obvious correlation (Fig. 8c), suggests alteration of most samples. In the pseudo-Van Krevelen diagram (Fig. 8d), samples describe a cluster of data with a type IV kerogen signature. This herein reinforces the hypothesis that most samples have been altered, probably weathered, and oxidised. Nevertheless, few samples having a type III kerogen signature will be discussed later in section 5.2 (Fig. 8d).

3.4. Monazite occurrences and geochemistry

Although accessory mineral, monazite may be observable in the field within the MOAT and UPLO formations (Fig. 9a, b). Because monazite is significantly dense (d=4.5), of large size (up to 1.5 mm) and resistant to weathering processes, heavy mineral grains, accumulated in several placers along the Aron and Gras rivers (Fig. 9c) where exploration works, mostly Banka drilling equipment, revealed heterogeneous concentrations (Donnot et al., 1973; Guigues and Sapinart, 1967). Heavy monazite grains mostly consist in grey nodules that are always hosted within a basal fertile gravel unit. Contents vary depending on the exploration sites between 400 and more than 5 000 g of monazite per m^3 of shales (*i.e.* ≈ 165 to >2 100 mg/kg, Fig. 9c). The richest sites are all localised along the northern limb of the Glévardais – Pont des Iles anticline axis. Contents are much lower south of the Sainte Anne sur Vilaine – Sions les Mines anticline axis (Fig. 9c). Note that the French Geological Survey (BRGM) produced 78 t of monazite concentrate from 1967 to 1968, while it operated La Monnerie placer deposit on a pre-industrial pilot-unit scale (Fig. 9d, e). These exploration works focused on the alluvial content in monazite nodules, but also provided some data on the average monazite content in shales (Fig. 9c). Besides that, exploration works (Guigues and Sapinart 1967) also highlighted that monazite-rich beds are correlated with fossiliferous and organic rich layers (Figs. 8b, 9c and 10a). Actually, grain distribution in rocks is not equally distributed in the whole area (Fig. 9c). Indeed, exploration works showed that the richest sites are rather localised in

the lower third of the MOAT formation and more particularly along the Glévardais – Pont des Iles anticline axis, where average monazite content is much larger than 200 mg/kg (*i.e.* >130 mg of REE per kg of shale; Lulzac, 1969).

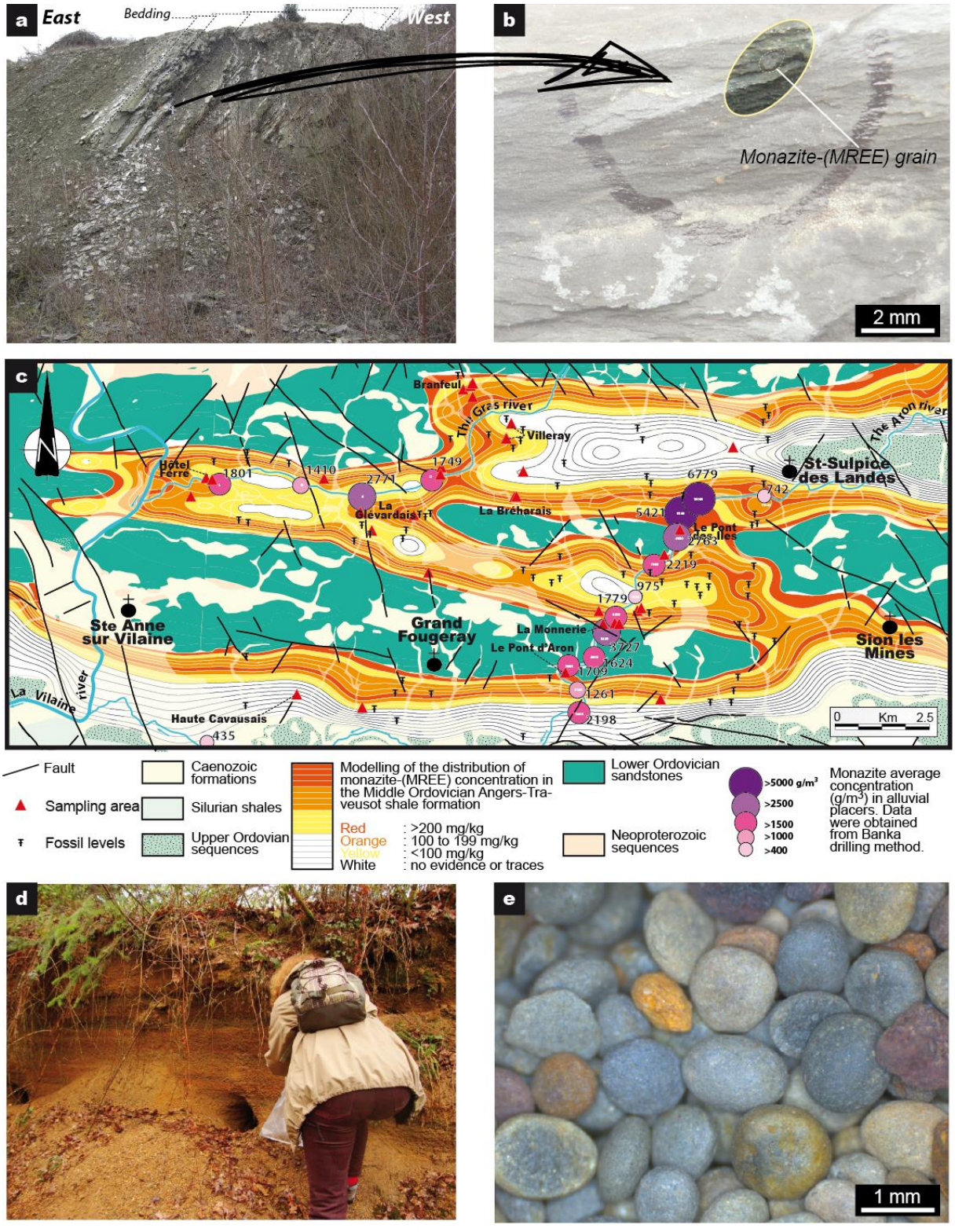

Fig. 9: Outcropping conditions of grey monazite nodule occurrences a) La Bréharais quarry and b) its large grey monazite nodular grain. Note this occurrence is localised along the fertile northern limb of the Glévardais – Pont des Iles anticline axis. The bedding roughly strikes E-W and dips to the north by approximately 40°. c) Modelling of the distribution of monazite nodule content in mg/kg within the MOAT formation. It consists of an interpolation between previous exploration data (Lulzac 1969) and potential-field interpolation method in which the shale formation has been separated into 18 stratigraphic sequences. Monazite concentration in alluvial placers reported by previous exploration works (Guigues and Sapinart 1967) are distributed into 5 different grade classes. d) Remaining monazite-rich sands from La Monnerie placer deposit operated between 1967 and 1968. e) Nodular grey monazite concentrate obtained from La Monnerie monazite-rich sands.

This thus explains the exceptional enrichment of alluvial placers in that area. It should be mentionned, however, these exploration data do not reflect those collected during this study in which we consider a median value for REE concentrations in shales close to 340 mg/kg, *i.e.* roughly equivalent to 500 mg of equivalent monazite per kg of shales. Of course, such an assumption thus supposes that the whole REE are carried by monazite and a 100% recovery rate during crushing, sifting and heavy media separation, regardless of grain size. Considering the differences between exploration works and this study, we herein suggest that REE-bearing monazite may also be of small-size that should make the recovery rate lower, and (or) that monazite are not the only REE-bearing phase.

Study of thin sections from rock samples, as well as polished sections of monazite concentrate from La Monnerie placer reveals 4 different monazite types all observed in the lower half of the MOAT and the UPLO formations.

Type 1 consists of typical NGM that forms elongate shapes, from sub-microscopic size to *ca.* 1.5 mm. Such nodules only occur in the lower anchizone of the MOAT formation where they are widespread, and also in rocks below belonging to the upper anchizone domain as for instance in Le Pont d'Aron. Elongate nodules develop rather parallel to the bedding (Fig. 10a and b). Nodules always are porous and display a poikilitic texture hosting numerous inclusions of phyllites, quartz, feldspar, rutile, graphite and iron oxides up to *ca*. 15 µm in size (Fig. 10b).

Raman analysis of several nodules do not reveal presence of rhabdophane (hexagonal $LREEPO_4.H_2O$) as previously suggested by Donnot et al. (1973). Nodules can also develop a chlorite-rich mantle that forms symmetric tails. Type 1 NGM also has a heterogeneous chemical composition with the following characteristics.

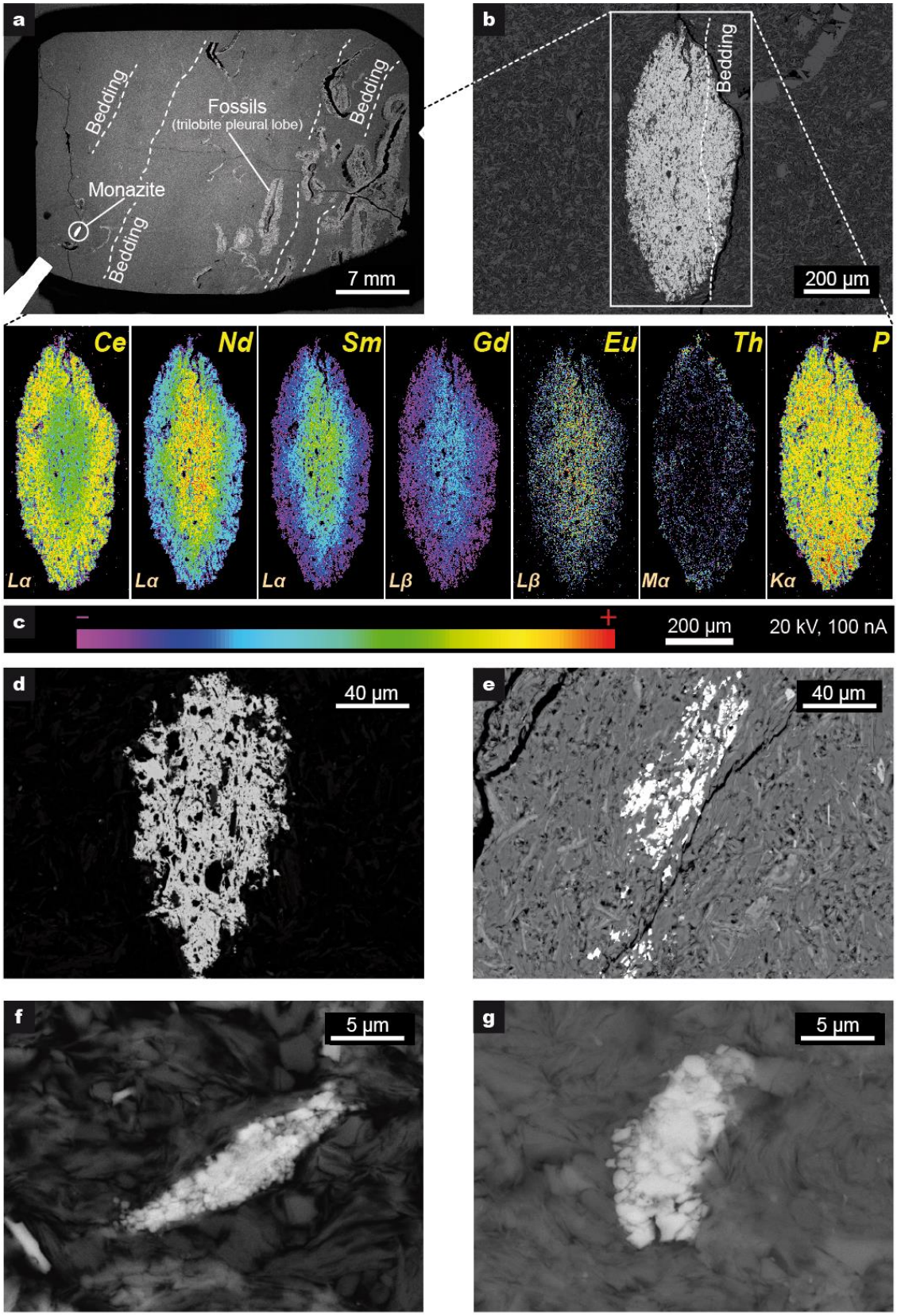

Fig. 10: Type 1 nodular grey monazite and small monazite grain geochemistry. a) Backscattered electron image of a thin section with a monazite module within a fossiliferous and TOC-rich shale. Sample GF12-06 from Branfeul. b) Backscattered electron image of a large monazite nodule. Note the

thin bedding parallel to the grain and the porous texture. Sample GF12-05 from Branfeul. c) Monazite nodule characterisation by EPMA mapping of Ce, Nd, Sm, Gd, Eu, Th and P. Sample GF12-05 from Branfeul. Backscattered electron images of small monazite grains from Branfeul d) sample GF12-05 and e) sample GF12-06, f and g) Cherhal (sample GF11-04).

Grains having size over 250 µm show typical core-rim chemical zoning (Fig. 10c), whereas smaller grains (<<200 µm) do not exhibit chemical zoning and show a complex assemblage of sub-micrometric nuclei (Fig. 10d-g). Concerning the largest nodules, their LREE contents (Fig. 11a-d and Appendix 4) are highly variable for Ce and Nd and La (0.27 to 0.51 *apfu*[1], 0.12 to 0.37 *apfu* and 0.05 to 0.25 *apfu*, respectively), and less for Pr (0.04 to 0.07 *apfu*). The chemical heterogeneity can be used to distinguished the end-member compositions. Nodule cores typically have a monazite-(Nd) to monazite-(Ce) composition whereas rims only display a monazite-(Ce) composition (Fig. 11e). In detail, NGM core composition differs from rim ones. Indeed, their Pr content gradually increases from monazite-(Nd) to -(Ce) end-members, whereas it gradually decreases in monazite-(Ce) rims (Fig. 11c).

Their Nd content also remains high (Fig. 11d-e). Note that smaller grains share similar features with core composition. They are enriched in Pr and have a typical monazite-(Ce) core composition. Such small monazite grains have been therefore assimilated and regarded as type 1 NGM core in graphs.

Note that both Ce and La contents increase toward monazite-(Ce) rims (Fig. 11a and b) whereas the Nd content is negatively correlated (Fig. 11d). The Pr content is very interesting as it describes a trend with a bell shape (Fig. 11c), and thus suggesting that core data are positively correlated with La and Ce, whereas rim data are negatively correlated. Relatively high amount of Sm (up to 0.14 *apfu*) with moderate amount of Gd (up to 0.06 *apfu*) and Eu (up to 0.02 *apfu*) is a characteristic feature of the type 1 NGM (Fig. 11f, g), with higher concentrations occurring in grain cores (up to 10.62 wt.% Sm_2O_3, 4.91 wt.% Gd_2O_3 and 1.31 wt.% Eu_2O_3). Y and Th contents are variable but generally low for monazite (0 to 0.51 wt.%

[1] *apfu* : atom per formula unit

Y_2O_3 with Me = 0.26 wt.%, and 0 to 1.49 wt.% ThO_2 with Me = 0.31 wt.%), and no clear distribution between both elements has been observed (Fig. 11h, i).

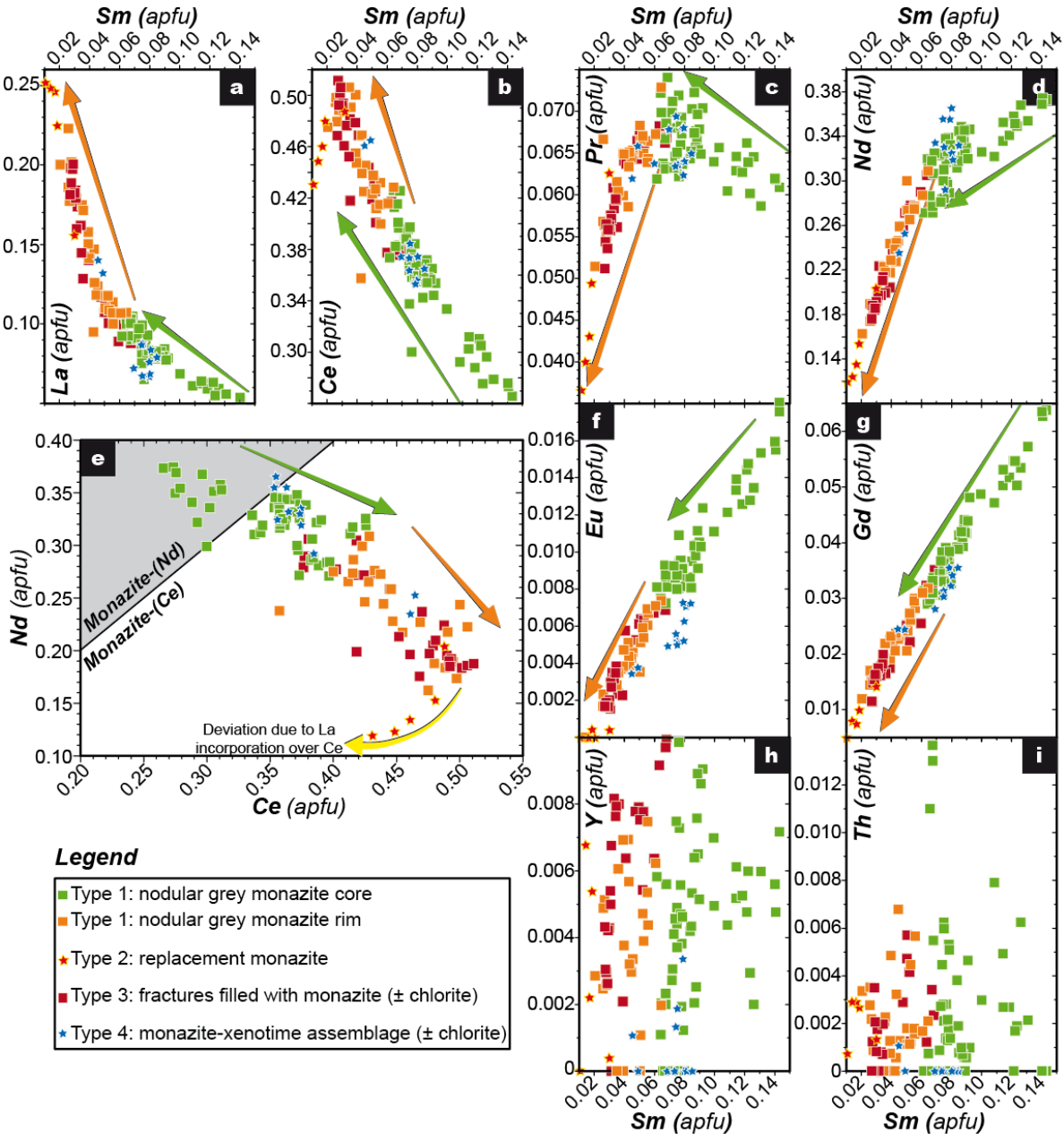

Fig. 11: Selected REE and Th in atom par formula unit (apfu) versus Sm, Ce (apfu) variation diagrams depicting a) La and b) Ce inverse relationships correlations, c) Pr bell shape behaviour, d) Nd, e) monazite end-member composition with respect to Nd and Ce, f) Eu, g) Gd positive correlations, and no correlation of Sm with h) Y and, i) Th.

By contrast, type 2 monazite consists of anhedral grains, with rare inclusions and shows replacement-recrystallization textures affecting type 1 NGM (Fig. 12a, b). Such a texture may be due to dissolution of type 1 NGM. Grains typically have a monazite-(Ce) composition (Fig. 11e) and become progressively enriched in La. This thus explains why type 2 monazite-(Ce) are the most enriched in Ce and La (0.43 to 0.49 *apfu* and 0.16 to 0.25 *apfu* respectively), and are depleted in Nd (0.12 to 0.2 *apfu,* Fig. 11a,b, d). They are also very weak in MREE with low Sm content (max: 0.03 *apfu*), and Gd content that are negligible (Fig. 11f, g). Chlorite may be related to the type 2 monazite-(Ce) paragenesis.

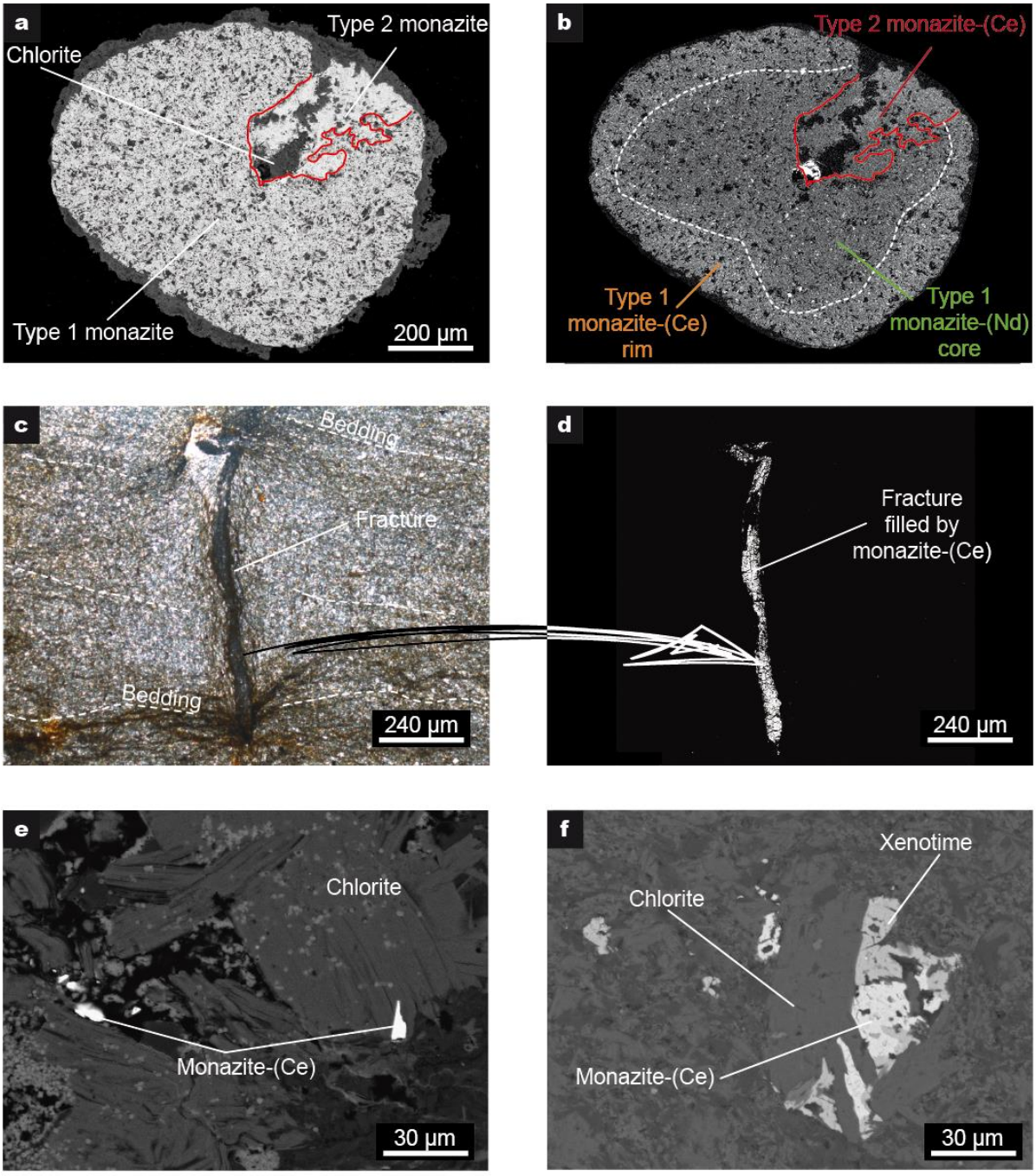

Fig. 12: Type 2 monazite geochemistry. a) Backscattered electron and b) cathodoluminescence imaging of a heavy grey monazite grain showing type 1 monazite-(Nd) core and monazite-(Ce) rim compositions, and also narrow re-entrant "corrosion" features filled with type 2 monazite-(Ce) and chlorite. Note the porous texture. Grain L5G3 on polished section, same scale. c) Plane polarized light microscopy of vein/fracture discordant with respect to the bedding and, d) filled by monazite-(Ce). Backscattered electron image, sample GF11-13 from Gras Richomme. e) Backscattered secondary electron image of a small monazite-(Ce) grain within chlorite sheets. Sample GF12-13 from Gras Richomme. f)

Backscattered secondary electron image of a thin section depicting a monazite, xenotime and chlorite paragenesis. Sample GF11-08 from Hôtel Ferré.

Type 3 monazite occurs as fracture/veinlet filling with chlorite (Fig. 12c, d, e). Grains also have a typical monazite-(Ce) composition and share common features with type 1 NGM rims (Fig. 11).

Type 4 monazite is related to a chlorite-rich paragenesis with xenotime (Fig. 12f). Such a monazite-xenotime assemblage has only been observed at Hôtel Ferré, which corresponds to the bottom part of the upper diagenetic domain (Fig. 5c). Note, no NGM has been seen observed in this sample. Type 4 monazite grains have heterogeneous chemical composition (Fig. 11) that evolves from monazite-(Nd) to monazite-(Ce). In detail, type 4 monazite may share some features with type 1 NGM cores as for instance for the enrichment in Pr, Nd, Sm or Gd, but appears as depleted in Eu and La. It has very low Y content, due to its unfavourable partition coefficient with respect to xenotime. Indeed, xenotime at equilibrium with this type 4 monazite have Y contents up to 41 wt.% Y_2O_3 (*i.e.* 0.78 *apfu*).

Monazite chemical zoning is well-illustrated in the UCC-normalized REE patterns (Fig. 13). The REE pattern of type 1 NGM cores suggests a bell-shape with a maximum in Sm (Fig. 13a). A very slight negative Eu anomaly may be suggested. Type 1 NGM rims are enriched in La and Ce and depleted in Nd-Gd with respect to type 1 NGM cores. Note that rims patterns have a relatively flat spectra with negative Eu anomaly. Type 2 monazite-(Ce) shows a pattern with a decreasing content from La to Gd with a very well-developed negative Eu anomaly (Fig. 13b). Type 3 monazite-(Ce) mimics the type 1 NGM rim pattern (Fig. 13c). Type 4 monazite patterns are superimposed to the field limits between type 1 NGM rims and cores (Fig. 13d), but display the negative Eu anomaly. By contrast, xenotime is depleted in LREE and enriched in MREE with a maximum in Eu (Fig. 13d). Y (*i.e.* HREE) is homogeneous and high.

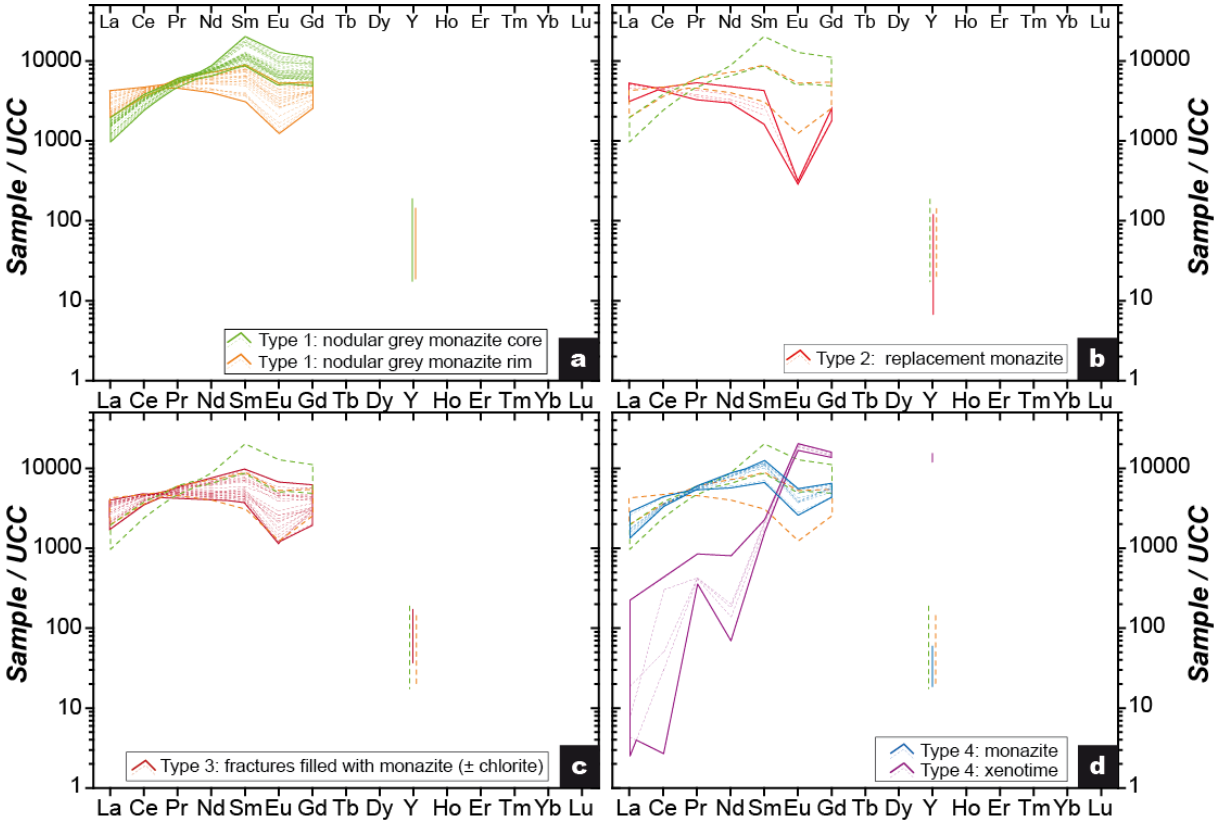

Fig. 13: UCC-normalised patterns of REE distribution for monazites. a) Electron-probe microanalysis of type 1 monazite nodule cores, and small grains and nuclei, and b) electron-probe microanalysis of type 1 monazite nodule rims and type 2 monazite grains. Inferred trends are deduced from LA-ICP-MS analysis from Jezequel 1993. UCC values are from McLennan (2001).

3.5. Monazite U/Pb geochronology

Although in situ U–Pb monazite dating is a sensitive method, age determination of NGM was challenged because of the combination of abundant host-rock inclusions and composition with low U content and significant non-radiogenic Pb. Analyses with the lowest U (and radiogenic Pb contents) below detection limits, were rejected from data processing and only appropriate results are used for age determination. To limit such artefacts, the change in the beam size from 10 to 15 µm also complicated the analysis of porous grains. Seventy nine analyses have been performed on four selected large heavy monazite grains (L2G7, L3G7, L4G9 and L5G3) from La Monnerie heavy concentrate (Appendix 6). Grain sizes range between 600 and 1500 µm. They display typical type 1 NGM core and rim zoning and display a typical porous-like/

inclusion-rich texture (Fig. 12a, b). Grains L2G7 and L5G3 also show replacement figures with type 2 monazite-(Ce) that is almost free of inclusions (Fig. 12a, b). Laser ablation inductively coupled plasma mass spectrometry (LA-ICP-MS) U–Pb geochronology of heavy monazite grain were performed at the BRGM laboratory with a nominal spot diameter of 15 µm whereas smaller monazite grains in thin section were analysed at the ISTO laboratory in order to achieve a higher resolution with a nominal spot diameter of 10 µm. Twenty-two analyses have been performed on monazite grains from two polished thin sections (GF11-13 and GF12-04). Grains in GF12-04 have type 1 NGM features and their sizes range between 200 and 400 µm. NGM grains in GF11-03 typically consist in type 3 monazite-(Ce) filling fractures (Fig. 12c, d). No dating has been undertook on type 4 monazite-xenotime assemblage because of their small size and scarcity.

The combined measured U-Pb data are reported in a Tera-Wasserburg diagram (Fig. 14).

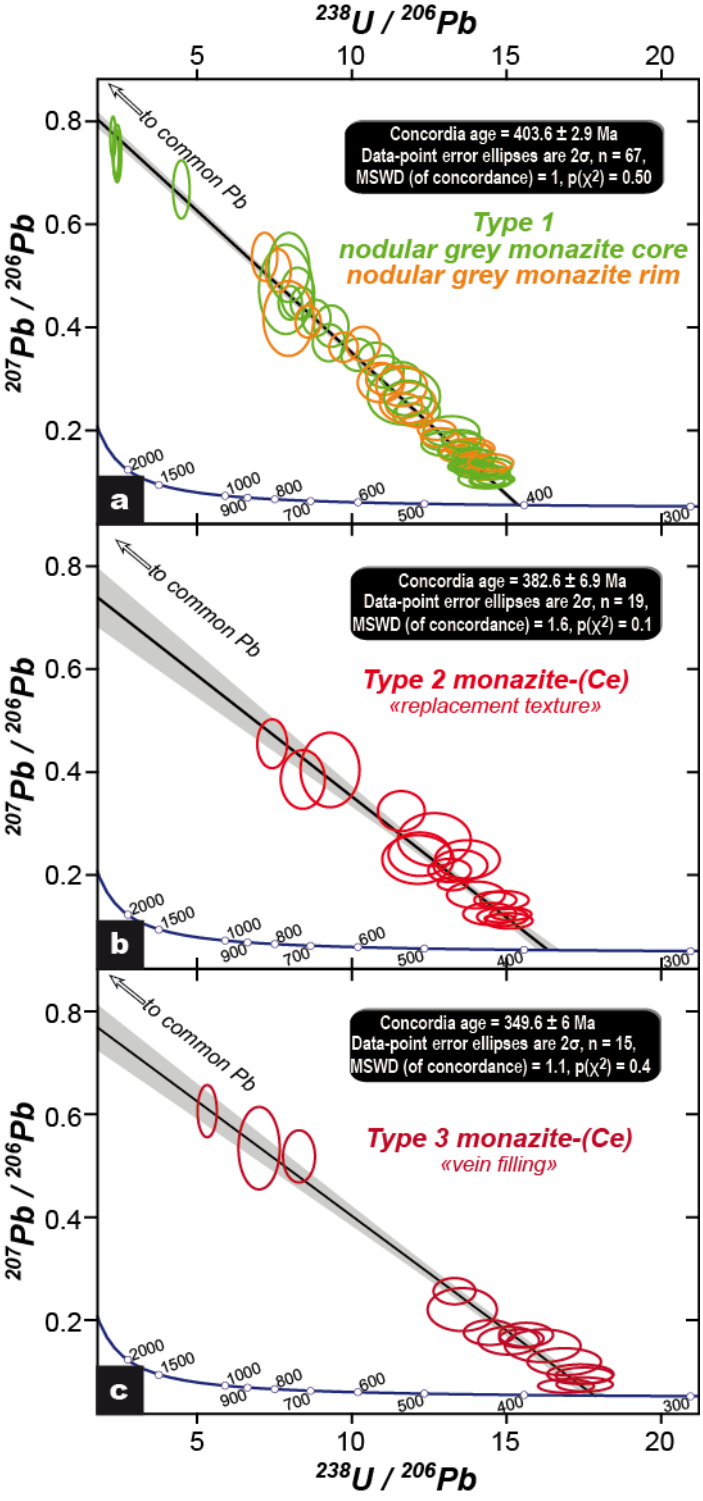

Fig. 14: U–Pb analyses obtained on heavy monazite grains. Tera & Wasserburg (1972) Concordia age calculated with the concordant data. Samples away from the concordia lines

are aligned along discordia lines and form isochrons for: a) type 1 nodular grey monazite-(Nd / Ce) cores and rim overgrowths, b) type 2 monazite-(Ce) displaying recrystallization-replacement textures on type 1 nodular grey monazite, and c) type 2 monazite-(Ce) in veins. MSWD, mean square of weighted deviation; p(χ2) mean Pearson's chi-squared test.

The analyses are typically discordant reflecting the incorporation of various amounts of common-Pb, but aligned well in a Tera-Wasserburg diagram (Fig. 14). According to textures and chemical compositions, three U-Pb age groups are highlighted.

i) Age group 1 was obtained in core and rim of type 1 monazite, which show variable Th/U ratio between 1.6 and 79.6 (average value at 14.4). Core and rim ellipses are well aligned and yield an age of 403.6 ± 2.9 Ma (MSWD=1; $p(\chi^2)$=0.5, Fig 14a).

ii) Age group 2 consists of type 2 monazite-(Ce). Th/U ratio also are heterogeneous with an average value at 10.7, and min and max values at 0.6 and 59.6 respectively. The 19 analyses gives an age at 382.6 ± 6.9 Ma (MSWD=1.6, $p(\chi^2)$=0.1, Fig 14b).

iii) Age group 3 consists of type 3 monazite-(Ce) observed in veins and fractures. Th/U ratio are low with an average value at 10.9 similar to type 2, and min and max values at 3.5 and 20.6 respectively. Intersection of the regression line with the Concordia gives and age at 349.6 ± 6 Ma (MSWD=1.1, $p(\chi^2)$=0.4, Fig 14c).

4. Discussion

4.1. The timing of the low-grade metamorphism event: a pre-Variscan geological setting

The KI variations herein show that sedimentary rocks from the Grand Fougeray area underwent very low-grade metamorphic conditions ranging from the upper diagenesis and lower anchizone in the MOAT formation to the upper anchizone in the UPLO formation. Epizonal conditions are assumed to occurs in the underlying Lower Ordovician and basement formations according to Le Corre (1975). Clays are dominated by smectite in the diagenesis domain, and illite in the anchizone one. Note that considering the Grand Fougeray area, these

conditions are generally consistent with those proposed by Le Corre (1975), but with no evidence of a regional metamorphic thermal anomaly trending N080°E as observed in this study. According to Gapais and Le Corre (1980), and Gumiaux et al. (2004), the structural pattern consists in bedding and cleavage distribution describing an upright fold system with *ca.* N110°E-trending fold axis. No clear correlation may be done between the metamorphic gradient distribution and the distance to the NBSASZ, *i.e.* the metamorphic gradient does not clearly increase when approaching the SASZ. Similarly, no correlation has been done between the metamorphic gradient distribution and the presence of a hidden granite including along the N080°E trending direction. Based on the 2D modelling of the MOAT formation folding using potential-field interpolation method and the intersection with a flat topography (the difference in height between the highest and lowest point is max. 50m, Fig. 5c), we herein show that metamorphic isograde follow the stratigraphic sequence and are folded. The MOAT formation thus reached its peak metamorphism prior to the Variscan folding event, possibly during burial of the basin sequences.

The KI may be used to approximate temperature ranges for metamorphic conditions (Frey, 1987) but it cannot be used as a precise geothermometer. Indeed, the temperature estimates for the KI boundaries between each metamorphic domains are based on comparison with other geothermometers derived from correlation with vitrinite reflectance data, conodont colour alteration index, fluid inclusion studies; thermodynamic modelling … (*e.g.* Ferreiro Mählmann, 2001; Ferreiro Mählmann and Frey, 2012; Merriman and Frey, 1999; Potel et al., 2006). Thus, temperatures for the metamorphic boundaries are approximately 215°C for upper diagenesis-lower anchizone, 250°C for mid-anchizone, and 295°C for upper anchizone-epizone, data that are in agreement with the equation from Zhu et al. (2016) work (Fig. 5a). From bottom to top, the Lower Ordovician sedimentary rocks (*i.e.* the Pont-Réan and Grés Armoricain formations) that occur in the Grand Fougeray area, including the UPLO formations underwent epizonal to upper anchizonal metamorphic conditions (this study and Le Corre, 1975). In detail, average temperature in the UPLO formation reaches *ca*. 264±16°C at Le Pont d'Aron. Above, the black-shales from the MOAT formation are affected, by lower metamorphic grades evolving from the

lower anchizone (= 227±7°C) toward the upper diagenesis conditions (= 170±23°C). The upper anchizone domain is thus assumed to roughly occur at the contact between the UPLO and the MOAT formations (Fig. 5c). The MOAT formation is, however, affected in its third lower part by lower anchizonal metamorphic grade corresponding to temperatures of between *ca*. 215°C and 250°C. Temperatures lower than *ca*. 215°C correspond to the upper two-third part of the MOAT formation that underwent upper diagenesis metamorphic conditions. Independently of palaeo-temperature estimations from KI values (Bignal et al., 2001; Zhu et al., 2016), one may question on the geothermal gradient occurring in the basin. Indeed, the MOAT formation is assumed to have been buried at shallow depth to a maximum of 2 to 2.5 km. Taking into account the palaeo-temperature estimations, then the attached estimated temperatures would require a rather abnormal geothermal gradient (*ca*. 75 to 100 °C/km in a lithostatic regime). Pochon et al. (2018) already suggest such a geothermal gradient in the CAD for a Sb hydrothermal system emplaced around 360 Ma, but for which they involved a thermal source in disequilibrium with country rocks such as heat advected by fluid flows. We herein suggest an anomalous thermal event prior to the Variscan deformation that may explain such a metamorphic gradient as explained below.

4.2. Diagenetic evolution of HC, clay dehydration, fluid circulations as processes for enhanced REE mobility

In the Grand fougeray area, the HC content of the MOAT black-shales is quite low (Fig. 8c), and in the pseudo-Van Krevelen diagram (Fig. 8d), samples describe clusters of data that spreads out along the type IV and more rarely type III kerogen fields. Because vascular plants are considered to have originated and adaptively radiated from the Silurian (Gensel 2008), a type III origin for the OM is precluded. This strongly reinforces the hypothesis that the OM has undergone severe alteration and oxidation stages. It is therefore reasonable to assume the original OM was at least fair to good, marine (*i.e.* phytoplankton) and terrestrial (*e.g.* spores) in origin. We therefore suggest that a type II kerogen underwent substantial oxidation during and after the thermal maturation as suggested by the oxidation trends pulling down-right the

data (Fig. 8d). Samples with low Oxygen Index (<<50 mg CO_2/g C_{org}) may be eventually interpreted as the less altered. The MOAT formation presently appears as over-mature sediments that have been oxidised just prior, but also after reaching the gas generation stage (Fig. 8d). According to Pepper and Corvi (1995), such a gas generation window would be effective in between *ca.* 140 and 210°C for dominantly marine organo-facies. Note that such a temperature range coincides with the upper diagenesis metamorphic grade as reached in the upper part of the MOAT formation.

Finally yet importantly, the MOAT formation trends to high K/Al (0.08 - 0.47) but have low K/Rb (142 – 250). According to Van de Kamp (2016), this may suggest rocks evolved in an open system and underwent K-metasomatism from hydrothermal fluids. The K source for such a metasomatism remains unknown event if we cannot preclude it may come from sandstones lenses or from the lower unit such as the Grés Armoricain, sandstone, formation. In the MOAT formation, the main K-bearing phases are clays and above all illite. Theses phases must be interpreted as the result of clay dehydration processes thus involving large and sudden volume changes related to water releasing with the loss of H_2O-layers. In detail and according to Vidal and Dubacq (2009), this process corresponds to successive incremental dehydration steps occurring during the burial of sediments. The greatest loss (~ 65 mol%) of water occurs between 40 and 220°C during which three breakdown reactions are modelled. The two first steps are assumed to occur during the lower diagenesis conditions (< 120°C). The third one occurs around 200-220°C, and is related to the release of 26 mol% water. Conversely, dehydration reactions pursue at higher temperatures although water release drastically decreases (Vidal and Dubacq, 2009). We may thus assume the upper diagenesis to lower anchizone diagenetic processes are assisted by fluid circulations implying in-source fluids released in response to clay dehydration reactions and most likely a more distal (deeper?) fluid source to explain K-metasomatism. Thus, fluid circulations prior to the Variscan deformation may thus explain the anomalous thermal gradient occurring in the basin. This process explains the type IV kerogen signature corresponding to a severe alteration / oxidation of the OM when entering in the gas window then after, during the ongoing thermal maturation. We may

therefore propose that REE mobility and NGM nucleation could be enhanced by dehydration steps and possible K-metasomatism occurring during burial.

4.3. Origins and timing of monazite

Both the UPLO and MOAT formations generally have a high REE content with average concentration close to 340 mg/kg. In domains free of alteration, this content seems to slightly increase with OM content (Figs 7a and 8b) and range from 250 to 550 mg/kg. Where the MOAT formation is altered and has underwent pore fluid migration processes (Fig. 7a), the REE content range is larger and may evolve from the lowest (175 mg/kg) to the highest concentration (1200 mg/kg, Fig 8b) in particular in the upper anchizonal part. The UCC normalized REE patterns are generally flat, with a moderate MREE enriched shapes for samples belonging to the diagenetic and lower anchizone domains of the MOAT formation (Fig. 7b, c) whereas a slight to high LREE enrichment is observed for samples belonging to the upper anchizone domain of the UPLO formation (Fig. 7d). Although the REE content in shales is rather constant in the UPLO and MOAT formations, monazite occurrences have been mostly observed in the anchizonal domain. Likewise, the source of heavy NGM grains from La Monnerie placer may only be the anchizonal shales that have been weathered and eroded upstream. In detail, type 1, 2 and 3 monazites only occur in the anchizonal domain, with one exception for type 4 monazite-xenotime assemblage that occurs in the lower part of the diagenetic domain, *i.e.* close to diagenesis-anchizone boundary. Note that such an observation was made in only one place at Hotel Ferré, and thus was not duplicated. These results are supported by exploration works in which an average monazite content much larger than 200 mg/kg (*i.e.* >130 mg of REE per kg of shale; Lulzac, 1969) has been evaluated in the anchizonal domain, the diagenetic one being almost barren. Thus monazite formation possibly associated with REE-enrichment is considered to occur at the anchizonal – diagenesis transition.

In the anchizone, type 1 NGM consists of typical grains and nodules that may be millimetric in size and that do not display euhedral habit (Fig. 10). They have irregular to ovoid elongate

shapes and are characterised by a porous texture in which numerous small mineral inclusions occur such as the ones observed in the surrounding shales. This textural evidence precludes a detrital origin and suggests an authigenic origin likely formed in response to fluid circulations, at the anchizonal transition. Moreover, the lack of detrital core and altered detrital monazite as well, thus precludes that NGM may be a product of fluid-assisted dissolution of detrital metamorphic monazite. Type 1 NGM grain zoning is complex and reveals a core enriched in MREE (and Nd) and rims in LREE (mostly Ce and La). NGM grains have a typical bell-shape UCC-normalised pattern enriched in MREE (Fig. 13a) although grain core has higher ratio than rim. Because of strong textural and compositional similarities between large nodular monazite grains and small grains and nuclei (Fig. 10), we assume that both textural assemblages belong to the same paragenesis. This thus questions on the growth model of grey monazite nodules. An aggregation model favouring high saturation and nucleation rates rather than the growth of a nanocrystal is herein suggested as observed for framboidal pyrite (Wilkin and Barnes, 1997). We herein suggest that NGM growth is the result of burial, increased temperature and fluid circulation, a concept that is reasonably well accepted (e.g. Burnotte et al., 1989; Milodowski and Zalasiewicz, 1991; Rasmussen and Muhling, 2007). The sources of REE and P, and reactions which produced authigenic NGM under conditions of very low-grade metamorphism are not well understood. They may be related to: (i) desorption of REE adsorbed on the surface of clay minerals during their diagenetic transformations (Burnotte et al., 1989; Milodowski and Zalasiewicz, 1991; Rosenblum and Mosier, 1983); (ii) desorption of REE and P during early diagenetic reductions of Fe oxides/hydroxides (Lev et al., 1998; März et al., 2008; Yang et al., 2017); (iii) degradation of OM (REE sorbed on the surface coatings or incorporated into biogenic material) in response to an early burial compaction (Evans and Zalasiewicz, 1996; Lev et al., 1998; März et al., 2008; Yang et al., 2017); (iv) dissolution of detrital REE-minerals including monazite as was described from greenschist-facies metasediments (Janots et al., 2008; Rasmussen and Muhling, 2007). Monazite distribution thus appears as controlled by different proxies of competing influences including fluid circulations as well. As thermal processes control OM maturation, clay transformation and fluid generation, NGM distribution

may be controlled by burial and depends on the metamorphic isograde distribution too. Despite the low OM content in MOAT formation (1 to 11 g/kg TOC; □ = 4 g/kg ± 2), both their REE and TOC contents present interesting correlations (Figs. 8b, 9c) with NGM occurrences that do not preclude OM to be important REE (and P) source. This assumption is reinforced knowing that both TOC and H (S_2 value) must decrease during sediment burial in response to the amount of reactive kerogen getting consumed (Fig. 8d). In any case, chemical composition (low Th, U, Y – HREE) zoning in REE observed in authigenic NGM from the MOAT formation, have already been assumed as typical for (very) low-grade metamorphic conditions (Alipour-Asll et al., 2012; Burnotte et al., 1989; Čopjaková et al., 2011; Donnot et al., 1973; Evans and Zalasiewicz, 1996; Evans et al., 2002; Halpin et al., 2014; Lev et al., 1998; Milodowski and Zalasiewicz, 1991; Rasmussen and Muhling, 2009). This thus questions if distinguish between both diagenetic and metamorphic-hydrothermal processes is possible, the KI appears as able to. We therefore assume that NGM appearance is a phenomenon that occurs at the diagenesis-lower anchizone transition. It also means that process may occur just prior and mostly within the gaz window.

The reason for the zoning observed in such low-T monazite is not fully elucidated up to date. It may be related to both REE and P evolution in pore fluid chemistry from early diagenesis to very low-grade metamorphism during increasing burial (Evans et al., 2002; Haley et al., 2004; Johannesson and Zhou, 1999; Kim et al., 2012; Lev et al., 1998; Milodowski and Zalasiewicz, 1991; Janots et al., 2008). Indeed, a shape bell REE pattern was observed in diagenetic fluids, and intensive P, LREE and MREE liberation into the sediment pore waters, and redistribution attributed to diagenetic processes is described in terrigenous sequences. Among the factors that control such processes, redox conditions at the water-sediment interface are of first importance (Dabard and Loi, 2012; März et al., 2008; Yang et al., 2017). The terrigenous MOAT formation corresponds to an outer shelf depositional environment (Henry, 1989). In such a deep environment, anoxic conditions are reached in a very short period of time preventing extensive phosphogenesis (apatite crystallization; Dabard and Loi, 2012; Jarvis, 1994). Under such oxygen-free conditions, OM respiration proceeds through the reactive

reduction of Fe-oxyhydroxides, a process that releases both P and REE to pore fluids (Freslon et al., 2014; Haley et al., 2004; März et al., 2008; Yang et al., 2017). Because compaction gradually reduces sediment porosity during burying, pore fluids cannot easily migrate toward the water-sediment interface anymore. We thus argue that deeper in the sediment during the upper diagenesis/anchizonal conditions, the ongoing release of P and REE with MREE enrichments from MO, Fe-oxyhydroxides and clays contributes in reaching monazite saturation in absence of CaO. Such low Ca contents with values below 5 g/kg CaO, are also typical for schists containing authigenic monazite (Čopjaková et al., 2011). Considering the chemical and thermodynamic features, Milodowski and Zalasiewicz (1991) suggest the REE migration as organic and bicarbonate complexes during diagenesis, and increasing stability of these complexes with increasing REE atomic number is responsible for zoning in the monazite nodules. However, solution complexation reactions involving organic, and/or the most common inorganic (carbonate, phosphate, hydroxide), ligands, leading to the general increase of solubility of REE from La to Lu in waters (Byrne and Lee, 1993; Lee and Byrne, 1992, 1993; Sonke and Salters, 2006; Wood, 1990), cannot fully explain observed zoning pattern (core–rim increase in La and Ce together with decrease in Nd + MREE). This way Burnotte et al. (1989) suggest zoning pattern can be explained by differences in the solubility of the individual REE phosphates. $REEPO_4$ solubility in aqueous solutions is poorly understood and some of them give conflicting results. Indeed, minimal solubility is observed for LREE between Ce and Sm; $LaPO_4$ solubility is substantially larger than neighbouring LREE and for HREE solubility increases with increasing atomic number (Liu and Byrne, 1997). And while, Pourret et al. (2007) further discuss the ability of organic acids to preferentially complex MREE, Van Hoozen et al., (2020) using thermodynamic calculations, suggest the Nd-(MREE)/Ce/La compositional changes record a gradual temperature increase during subsequent growth. Lazareva et al. (2018) which focus on hydrated REE-phosphate precursor point out the role of Eh–pH variations.

We therefore suggest the precipitation of type 1 monazite core (Nd to Ce compositions) occurs in the upper diagenesis, within the gaz window (140-210°C), and under reducing conditions

from slightly acidic to near neutral fluid pH that favour MREE incorporation. The REE's source is driven by the competing influences of the refractory organic (MREE to HREE), Fe-oxyhydroxides (P, Ce and MREE) and siliciclastic fractions (L to HREE). Type 1 monazite rim evolving toward Ce compositions is assumed to be the result of progressive increasing temperature that reaches the lower anchizone facies. NGM crystallisation is herein assumed to begin in the upper diagenenesis, and end in the lower anchizone. Such a formation process occurs around 405-400 Ma, a period that may correspond to the diagenesis-anchizone transition. This date is in agreement with SHRIMP U/Pb ages on authigenic grey monazite from the Llandovery strata in central Wales (Evans et al., 2002). There, such an age has been also interpreted as being diagenetic and dating compactional dewatering associated with the rocks passing though the smectite–illite transition during hydrocarbon expulsion. This thus reinforces that NGM crystallisation occurs under ongoing and evolving physico-chemical conditions in response to reductive dissolution of OM maturation and Fe-oxyhydroxides.

By contrast, type 2 and type 3 monazite-(Ce) grains may be anhedral or sub-euhedral and mostly micrometric in size, except when filling fractures. Type 2 monazite is distinctive in compositions and its textural positions indicate that it postdates type 1 monazite. Indeed, type 1 NGM (core and rim) has been partially dissolved and replaced to type 2 monazite-(Ce). Type 3 monazite shows microtextures suggesting syn-metamorph monazite formation linked to deformation of basin sediments similarly as Wilby et al. (2007). Both type 2 and type 3 monazite-(Ce) are late in the mineral paragenesis and are also assumed to form in the anchizonal conditions. Type 2 replacement monazite forms at *ca.* 385-375 Ma whereas type 3 vein filling emplaced later *ca*. 350 Ma. Both monazite types may correspond to an open-system REE redistribution during regional deformation stages.

Because it has been observed at one time, the processes at the origin of the type 4 monazite-xenotime assemblage cannot be easily explained. Focusing on the HREE behaviour, one can note that REE adsorbed on siliciclastic fractions are mainly represented by clays on which HREE are more sorbed than LREE (Coppin et al., 2002). Similarly, entering the gas window is assumed to release more HREE from OM (Yang et al., 2017). Hence, the ongoing dehydration

processes affecting clays and the OM maturation are assumed to release in the microporosity both water and the refractory HREE at the end of the diagenesis during the methanogenesis stage to form the monazite-xenotime. The diagenetic signature of type 4 monazite may expressed in the MREE and Nd enrichment.

Considering Pr distribution, the Pr versus Sm plot (Fig. 11c) suggests different behaviours during grain growth with respect to the positive and negative slope trends, this element may be of interest to evaluate the possible processes at the origin of monazite nucleation. Europium, as well, may be herein considered as the MREE proxy. The variability in the REE patterns (Fig. 13) correlates well with Pr_{UCC} versus $Log(La/Sm)_{UCC}$ (Fig. 15). According to the abovementioned results, we herein suggest that core compositions of type 1 NGM with the lowest ratio values may crystallise in the upper diagenesis conditions, whereas rim overgrowths may develop in the anchizone conditions. Monazite grain low Pr_{UCC} content and highest $Log(La/Sm)_{UCC}$ ratio may correspond metamorphic and magmatic monazites.

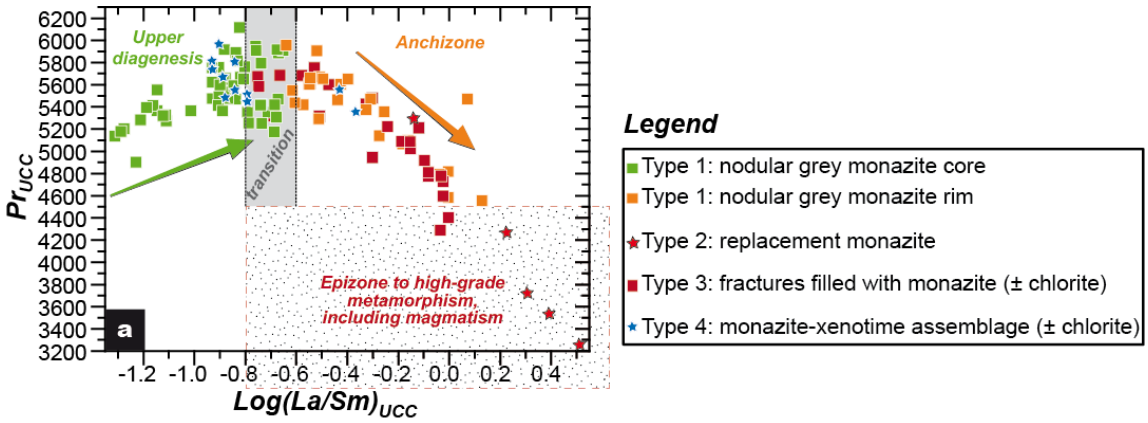

Fig. 15: $(Pr)_{UCC}$ vs $Log(La/Sm)_{UCC}$ for the different generations of monazites showing REE fractionation during grain growth and overgrowths. The hatched area that can go beyond the graph limit, represents composition field of most metamorphic and magmatic monazites. UCC values are from McLennan (2001).

The in between conditions corresponding to the apex with respect to Pr contents may correspond to change between diagenetic and hydrothermal-metamorphic processes that

occur during anchizonal conditions. Type 2 replacement monazite with the highest $Log(La/Sm)_{UCC}$ ratio values, corresponds to higher metamorphic grades thus questioning if a localised elevation of temperature may have occurred (e.g. fluid circulation along faults and fractures). As usual, type 3 monazite in vein mimics the NGM rim trend.

4.4. The formation of grey monazite nodule in high heat flux: a link with geodynamic setting?

The MOAT formation emplaced in an outer shelf environment dominated by black-shales depositions from 470 to 460 Ma (Fig. 16a). In such an environment, Pourret and Tuduri (2017) reassessed the REE external cycle and explained that because a seawater-like REE pattern already occurs in the truly dissolved pool of river input, the seawater REE-pattern thus results in a combination of both intra-oceanic and riverine processes. As a consequence, during the transfer of stream water to the oceans 90% of REE are removed from the solution by flocculation of colloidal materials that are then trapped and sedimented on the sea-floor. Pourret and Tuduri (2017) thus consider continental shelves as potential REE traps, and shelf sediments compared to metalliferous deep sea sediments (Kato et al., 2011). We explain below the formation of grey monazite nodule is linked to the earlier building of the Variscan belt and is especially dependant to the thermal evolution of the upper crust, and REE remobilisation (as Type-2 replacement or type-3 monazite in late fractures) develops in response to regional deformation and fluid circulations. Indeed, the U/Pb dates (Fig. 14) recorded by the different generations of monazites reveal a long lasting process that initiated at the onset of the Devonian and ceased during the lower Carboniferous. The precipitation of NGM begun *ca.* 50 My after the deposition of the whole Middle Ordovician Angers-Traveusot sedimentary sequences (Fig. 16a). More broadly, nodular grey monazite-(Nd core to Ce rim) formed *ca*. 405-400 My ago during the Lower Devonian (Emsian). In detail, this Lower Devonian event matches with the earliest phase of the Variscan convergence (Fig. 16b) evidenced South of the CAD by the setting up of a northward subduction and the development of the Saint-Georges-sur-Loire Devonian volcanic back-arc basin (Figs. 1) that also emplaced

around 420-400 Ma (Ballèvre et al., 2009; Ducassou et al., 2011; Ducassou et al., 2014; Tartèse et al., 2015). This thinning was accommodated by asthenospheric upwelling, inducing a large heat flux at the base of the crust that boosts the thermal evolution of the sediments, the OM maturation, MREE, P and water releasing conducive to the NGM precipitation in conditions belonging to the upper diagenesis to anchizone. Note that in the central Welsh Basin, NGM may form during the Lower Devonian as well (417 ± 11 Ma U/Pb isotope dilution, Evans & Zalasiewicz, 1996)

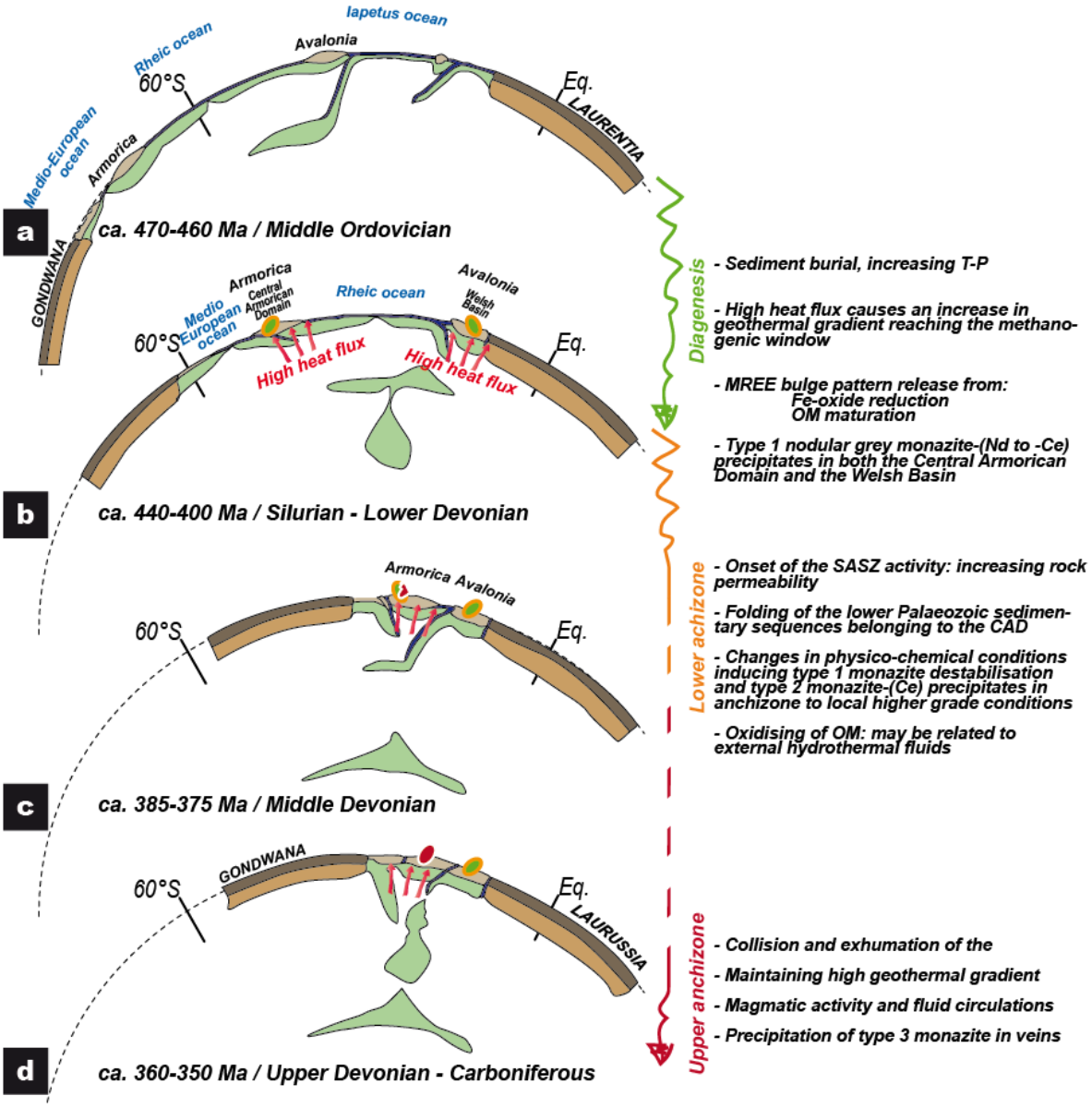

Fig. 16: Interpretative cross-section of the plate scale geodynamic setting between both the Gondwana and Laurentia-Laurussia margins showing the timing of formation of nodular grey monazite in the Central Armorican Domain and in the Welsh Basin (after Ducassou et al., 2014; Tartese et al., 2015 and Vanderhaeghe et al., 2020). a) Middle Ordovocian and since the Cambrian: the margin of Gondwana is marked by hyperextension conducive to the formation of Avalonia and Armorica with the opening of the Rheic ocean then the Medio-European Ocean, and the closure of the Iapetus ocean. b) Silurian to Lower Devonian: The Avalonia has been accreted to the Laurentia and the Rheic ocean initiates its subduction beneath the Laurussia. The Medio-European Ocean also started to subduct beneath the Armorica. Around 405-400 Ma, the diagenesis supported by a high-heat flux probably favoured the precipitation of nodular grey monazite in a back-arc setting. c) Middle Devonian: oceanic domains are pretty closed and the Armorica is bounded by subduction zones. This event is related to the earlier stages of the Variscan belt such as the onset of the South Armorican Shear Zone activity and folding of the lower Palaeaozoic formations. Note the high heat flux may appear as persistent in the Central Armorican Domain due to the two opposite-verging subduction zones and may destabilise nodular monazite grain into metamorphic monazite. d) Upper Devonian – Lower carboniferous: the Variscan orogenic front evolves in association association with slab retreat and orogenic gravitational collapse inducing ongoing high heat flux in the Central Armorican Domain and development of metamorphic monazite.

The ongoing northward subduction of the South-Armorican Massif Central Ocean is followed by the progressive accretion of allochthons terranes (oceanic units and outer margin of Gondwana) and the earliest phase of folding in the Central Armorican Domain of interest herein at *ca*. 385 Ma (Fig. 16c). Such a setting may be consistent with the persistence of heat fluxes above the continental subduction panel probably maintained by a two opposite-verging subduction zones as a result of both the closure of the Medio-European and Rheic oceans (Vanderhaeghe et al., 2020). Type 2 replacement monazite develops *ca*. 385-375 My ago at the transition during the Middle and Upper Devonian (Givetian / Frasnian), a period that corresponds to the early Variscan deformation stage (folding, cleavage, faulting) that probably increases rock permeability and favours fluid circulations and veining in the lower part of MOAT formation and the oxidizing of the OM as well. Fluid circulations of mixed sources may also

explain replacement process. The metamorphic conditions also correspond to the anchizone domain, although some very high $Log(La/Sm)_{UCC}$ and low Pr_{UCC} may suggest that local epizonal condition has occured. Note that Tuduri et al. (2014) provided an U/Pb ID-TIMS age of 384 ± 1.6 Ma for expected type 1 nodular monazite grain from La Monnerie concentrate. Such a date is herein reinterpreted and heavy grains are considered are replaced by type 2 monazite.

Later stages correspond to the main exhumation of the subducted Gondwanian crust, and nappe stacking, south of the CAD at *ca.* 360-350 Ma (Fig. 16d) and possibly the partial exhumation of the MOAT formation due to folding. Overall, the CAD remains rather unscathed from major Variscan deformation stages during these stages but it does not preclude high heat flow, fluid circulations and monazite depositions (Gloaguen et al., 2007; Pochon et al., 2018; Tartèse et al., 2015). Consequently, late type 3 monazite related to veining crystallises *ca*. 350 My ago during the Mississipian (Tournaisian).

5. Concluding remarks

In the Grand-Fougeray area, the Middle Ordovician Angers-Traveusot black-shale formation reached peak metamorphism in the lower anchizone facies prior to the Variscan folding event. Nodular grey monazite belongs to -Nd and -Ce endmembers with a severe zoning in MREE. They are formed in response to diagenetic to anchizonal processes and are assumed to be stable from 140°C to *ca.* 250°C. REE were redistributed into core and rim of nodular grey monazite by a series of diagenetic processes controlled by different proxies of competing influences such as the OM maturation, Fe oxide/hydroxide, clay transformation, and fluid circulations during the Lower Devonian *ca.* 405 to 400 Ma.

Later stages are related to compressional deformation that occurs from 385 to 350 Ma and consist in the precipitation of monazite-Ce in the anchimetamorphism domain as well. The geodynamic setting therefore has strong influence on the nodular grey monazite crystallisation as it catalysed the thermal maturation of both sediments and OM in a back-arc setting. Such a thermal input may be also considered in many other settings where nodular grey monazite

always occurs at the onset of mountain building or in the distal thermal aureole of magmatic intrusion (Alipour-Asll et al., 2012; Lazareva et al., 2018; Rosenblum and Mosier, 1983; Wing et al., 2003).

Consequently, palaeocontinental shelves may be considered as traps for potential REE resources and thus interesting guides for the exploration as suggested by Pourret and Tuduri (2017). Although, authigenic nodular grey monazite occurrences do not appear as interesting for economic considerations, heavy nodules may constitute an interesting by-products for the mineral sands industry as the REE became intensively use in a wide range of low carbon energy production processes and high-technology devices. Indeed, the typical association of common monazite-Ce with radioactive elements such as Th and sometimes U, constitutes an important barrier to project development.

Many occurrences of nodular grey monazite are known in Americas, Asia, Europe and Africa (Rosemblum and Mosier 1983; Charles et al., 2022) and future studies may explain they are control by high heat flux that may be due to a specific geodynamical setting or to local heat flow redistribution such as in thermal haloes around magmatic intrusions.

The nodular grey monazite with MREE-rich patterns thus constitutes an interesting alternative solution because of its very low content in both Th and U and negligible radiological impact if mining (Donnot et al., 1973; García-Tenorio et al., 2018; Rosenblum and Mosier, 1983; Tuduri et al., 2015). At present, placers only display some limited economical interest.

Author Contributions:

Acknowledgements: The work was developed within the ASTER project, supported by the French National Research Agency; ANR (project ANR-11-ECOT-002). Many thanks to Kensaï Artis, Alexandre Borniche, Faddy Nassif, Pierre-Marie Bastien, Léo Thévenin, Baptiste Vincens and Sébastien Potel for their contributions to the XRD analysis, to Mohammed Boussafir for his precious comments on Rock-EVAL interpretation and to Jérémie Melleton for discussions on the ages.

Conflicts of Interest: The authors declare no conflict of interest.

References

Alipour-Asll, M., Mirnejad, H., Milodowski, A.E., 2012. Occurrence and paragenesis of diagenetic monazite in the upper Triassic black shales of the Marvast region, South Yazd, Iran. Mineral. Petrol. 104, 197-210.

Ballèvre, M., Bosse, V., Ducassou, C., Pitra, P., 2009. Palaeozoic history of the Armorican Massif: Models for the tectonic evolution of the suture zones. C. R. Geosci. 341, 174-201.

Bea, F., 1996. Residence of REE, Y, Th and U in granites and crustal protoliths; Implications for the chemistry of crustal melts. J. Petrol. 37, 521-552.

Brun, J.P., Guennoc, P., Truffert, C., Vairon, J., 2001. Cadomian tectonics in northern Brittany: a contribution of 3-D crustal-scale modelling. Tectonophysics 331, 229-246.

Burnotte, E., Pirard, E., Michel, G., 1989. Genesis of gray monazites; evidence from the Paleozoic of Belgium. Econ. Geol. 84, 1417-1429.

Byrne, R.H., Lee, J.H., 1993. Comparative yttrium and rare earth element chemistries in seawater. Marine Chemistry 44, 121-130.

Calcagno, P., Chilès, J.P., Courrioux, G., Guillen, A., 2008. Geological modelling from field data and geological knowledge: Part I. Modelling method coupling 3D potential-field interpolation and geological rules. Phys. Earth Planet. Inter. 171, 147-157.

Chantraine, J., Autran, A., Cavelier, C., Clozier, L., 2003. Carte géologique de la France à l'échelle du millionième, 6e édition révisée ed. BRGM, Orléans, France.

Charles, N., Tuduri, J., Lefebvre, G., Pourret, O., Gaillard, F., Goodenough, K., 2022. Ressources en terres rares de l'Europe et du Groenland : un potentiel minier remarquable mais tabou ?, in: Decrée, S., Boulvais, P. (Eds.), Ressources métalliques : cadre géodynamique et exemples remarquables. ISTE Science Publishing Ltd, Wiley.

Choukroune, P., Lopez-Munoz, M., Ouali, J., 1983. Cisaillement ductile sud-armoricain et déformations discontinues associées: mise en évidence de la déformation régionale non coaxiale dextre. Comptes Rendus - Academie des Sciences, Serie II 296, 657-660.

Cobert, C., Baele, J.-M., Boulvais, P., Decrée, S., Dupont, N., Spagna, P., 2015. Grey monazite paleoplacers in Lower Cretaceous continental formations in the Mons Basin, Belgium, SGA2015: 13th Biennial meeting, pp. 1173-1176.

Cooper, D.C., Basham, I.R., Smith, T.K., 1983. On the occurrence of an unusual form of monazite in panned stream sediments in Wales. Geol. J. 18, 121-127.

Čopjaková, R., Novák, M., Franců, E., 2011. Formation of authigenic monazite-(Ce) to monazite-(Nd) from Upper Carboniferous graywackes of the Drahany Upland: Roles of the chemical composition of host rock and burial temperature. Lithos 127, 373-385.

Coppin, F., Berger, G., Bauer, A., Castet, S., Loubet, M., 2002. Sorption of lanthanides on smectite and kaolinite. Chem. Geol. 182, 57-68.

Dabard, M.P., Loi, A., Paris, F., Ghienne, J.F., Pistis, M., Vidal, M., 2015. Sea-level curve for the Middle to early Late Ordovician in the Armorican Massif (western France): Icehouse third-order glacio-eustatic cycles. Palaeogeogr. Palaeoclimatol. Palaeoecol. 436, 96-111.

Dabard, M.-P., Loi, A., 2012. Environmental control on concretion-forming processes: Examples from Paleozoic terrigenous sediments of the North Gondwana margin, Armorican Massif (Middle Ordovician and Middle Devonian) and SW Sardinia (Late Ordovician). Sediment. Geol. 267-268, 93-103.

Dabard, M.-P., Loi, A., Paris, F., 2007. Relationship between phosphogenesis and sequence architecture: Sequence stratigraphy and biostratigraphy in the Middle Ordovician of the Armorican Massif (NW France). Palaeogeogr. Palaeoclimatol. Palaeoecol. 248, 339-356.

Dadet, P., Herrouin, Y., Blanchet, C., Bardy, P., Colleau, A., 1995. Carte géol. France (1/50000), feuille Pipriac (387). BRGM, Orléans, France.

Dadet, P., Herrouin, Y., Laville, P., Paris, F., 1987. Carte géol. France (1/50000), feuille Bain-de-Bretagne (388). BRGM, Orléans, France.

Donnot, M., Guigues, J., Lulzac, Y., Magnien, A., Parfenoff, A., Picot, P., 1973. Un nouveau type de gisement d'europium: la monazite grise à europium en nodules dans les schistes paléozoïques de Bretagne. Miner. Deposita 8, 7-18.

Ducassou, C., Ballèvre, M., Lardeux, H., Robin, C., 2011. Evidence for pre-orogenic, Early Devonian rifting in the Variscan belt: stratigraphy and structure of the Palaeozoic cover of the Mauges Unit (Upper Allochthon, Armorican massif, France). Int. J. Earth Sci. 100, 1451-1475.

Ducassou, C., Poujol, M., Ruffet, G., Bruguier, O., Ballèvre, M., 2014. Relief variation and erosion of the Variscan belt: detrital geochronology of the Palaeozoic sediments from the Mauges Unit (Armorican Massif, France). Geol. Soc. London Spec. Publ. 405, 137.

Durand, J., Noblet, C., 1986. Paléocourants dans la Formation du Grès armoricain: persistance des mécanismes de transport en domaine cratonique. Rev. Géol. Dyn. Géogr. Phys. 27, 13-26.

Engi, M., 2017. Petrochronology based on REE-minerals: monazite, allanite, xenotime, apatite. Rev. Mineral. Geochem. 83, 365-418.

Evans, J., Zalasiewicz, J., 1996. U-Pb, Pb-Pb and Sm-Nd dating of authigenic monazite: implications for the diagenetic evolution of the Welsh Basin. Earth Planet. Sci. Lett. 144, 421-433.

Evans, J.A., Zalasiewicz, J.A., Fletcher, I., Rasmussen, B., Pearce, N.J.G., 2002. Dating diagenetic monazite in mudrocks: constraining the oil window? J. Geol. Soc. 159, 619.

Ferreiro Mählmann, R., 2001. Correlation of very low grade data to calibrate a thermal maturity model in a nappe tectonic setting, a case study from the Alps. Tectonophysics 334, 1-33.

Ferreiro Mählmann, R., Frey, M., 2012. Standardisation, calibration and correlation of the Kübler-index and the vitrinite/bituminite reflectance: an inter-laboratory and field related study. Swiss Journal of Geosciences 105, 153-170.

Freslon, N., Bayon, G., Toucanne, S., Bermell, S., Bollinger, C., Chéron, S., Etoubleau, J., Germain, Y., Khripounoff, A., Ponzevera, E., Rouget, M.-L., 2014. Rare earth elements and neodymium isotopes in sedimentary organic matter. Geochim. Cosmochim. Acta 140, 177-198.

Frey, M., 1987. Low Temperature Metamorphism, in: Frey, M. (Ed.), Frey, M. (ed.)(1987): . , Glasgow and London, 351 pp. Frey, M., Desmons, J. and Neubauer, F. (eds.) ed. Blackie & Son Limited, Glasgow, London, p. 351.

Gapais, D., Brun, J.-P., Gumiaux, C., Cagnard, F., Ruffet, G., Le Carlier De Veslud, C., 2015. Extensional tectonics in the Hercynian Armorican belt (France). An overview. Bull. Soc. Geol. Fr. 186, 117-129.

Gapais, D., Le Corre, C., 1980. Is the Hercynien belt of Brittany a major shear zone? Nature 288, 574-576.

García-Tenorio, R., Manjón, G., Vioque, I., Jiménez-Ramos, M.C., Mantero, J., Díaz-Francés, I., 2018. Grey monazite (rare earths) mining in centre of Spain: Characterization and pre-operational radiological evaluation. Chemosphere 208, 691-697.

Gensel, P.G., 2008. The Earliest Land Plants. Annual Review of Ecology, Evolution, and Systematics 39, 459-477.

Gloaguen, E., Branquet, Y., Boulvais, P., Moëlo, Y., Chauvel, J.-J., Chiappero, P.-J., Marcoux, E., 2007. Palaeozoic oolitic ironstone of the French Armorican Massif: a chemical and structural trap for orogenic base metal–As–Sb–Au mineralisation during Hercynian strike-slip deformation. Miner. Deposita 42, 399-422.

Guggenheim, S., Bain, D.C., F. Bergaya, u., Brigatti, M.F., Drits, V.A., Eberl, D.D., Formoso, M.L.L., Galán, E., Merriman, R.J., Peacor, D.R., Stanjek, H., Watanabe, T., 2002. Report of the Association Internationale pour l'Etude des Argiles (AIPEA) Nomenclature Committee for 2001: Order, disorder and crystallinity in phyllosilicates and the use of the 'Crystallinity Index'. Clay Miner. 37, 389-393.

Guigues, J., Devismes, P., 1969. La prospection minière à la batée dans le Massif Armoricain: méthodes, résultats, atlas minéralogique. Mémoires du BRGM 71, 167.

Guigues, J., Sapinart, J., 1967. Monazite à europium armoricaine. Résumé des travaux effectués et état des connaissances au 28.2.1967. BRGM, p. 40.

Guillocheau, F., Rolet, J., 1982. La sedimentation paleozoique ouest-armoricaine; histoire sedimentaire; relations tectonique-sedimentation. Bull. Soc. Géol. Minéral. Bretagne 14, 45-62.

Gumiaux, C., Gapais, D., Brun, J.P., Chantraine, J., Ruffet, G., 2004. Tectonic history of the Hercynian Armorican Shear belt (Brittany, France). Geodin. Acta 17, 289-307.

Guyonnet, D., Planchon, M., Rollat, A., Tuduri, J., 2016. Dynamic representation of flows and stocks of metals in the Economy in: Chagnes, A., Cote, G., Ekberg, C., Nilsson, M., Retegan, T. (Eds.), WEEE Recycling: research, development, and policies. Elsevier, pp. 31-52.

Haley, B.A., Klinkhammer, G.P., McManus, J., 2004. Rare earth elements in pore waters of marine sediments. Geochim. Cosmochim. Acta 68, 1265-1279.

Halpin, J.A., Jensen, T., McGoldrick, P., Meffre, S., Berry, R.F., Everard, J.L., Calver, C.R., Thompson, J., Goemann, K., Whittaker, J.M., 2014. Authigenic monazite and detrital zircon dating from the Proterozoic Rocky Cape Group, Tasmania: Links to the Belt-Purcell Supergroup, North America. Precambrian Res. 250, 50-67.

Henderson, P., 1984. Rare earth element geochemistry. Elsevier, Amsterdam, NL.

Henry, J.-L., 1989. Paléoenvironnements et dynamique de faunes de Trilobites dans l'Ordovicien (Llanvirn Supérieur-caradoc basal) du Massif Armoricain (France). Palaeogeogr. Palaeoclimatol. Palaeoecol. 73, 139-153.

Herron, M.M., 1988. Geochemical classification of terrigenous sands and shales from core or log data. J. Sediment. Res. 58, 820-829.

Janots, E., Berger, A., Engi, M., 2011. Physico-chemical control on the REE minerals in chloritoid-grade metasediments from a single outcrop (Central Alps, Switzerland). Lithos 121, 1-11.

Janots, E., Engi, M., Berger, A., Allaz, J., Schwarz, J.O., Spandler, C., 2008. Prograde metamorphic sequence of REE minerals in pelitic rocks of the Central Alps: implications for allanite–monazite–xenotime phase relations from 250 to 610°C. J. Metamorph. Geol. 26, 509-526.

Jarvis, I., 1994. Phosphorite geochemistry: state-of-the-art and environmental concerns. Eclogae Geologicae Helvetiae 87, 643-700.

Jégouzo, P., 1980. The South Armorican Shear Zone. J. Struct. Geol. 2, 39-47.

Johannesson, K.H., Stetzenbach, K.J., Hodge, V.F., 1997. Rare earth elements as geochemical tracers of regional groundwater mixing. Geochim. Cosmochim. Acta 61, 3605-3618.

Johannesson, K.H., Zhou, X., 1999. Origin of middle rare earth element enrichments in acid waters of a Canadian High Arctic lake. Geochim. Cosmochim. Acta 63, 153-165.

Jones, A.P., Wall, F., Williams, C.T., 1996. Rare earth minerals. Chemistry, origin and ore deposits. Chapman & Hall, London, UK.

Kato, Y., Fujinaga, K., Nakamura, K., Takaya, Y., Kitamura, K., Ohta, J., Toda, R., Nakashima, T., Iwamori, H., 2011. Deep-sea mud in the Pacific Ocean as a potential resource for rare-earth elements. Nat. Geosci. 4, 535-539.

Kim, J.-H., Torres, M.E., Haley, B.A., Kastner, M., Pohlman, J.W., Riedel, M., Lee, Y.-J., 2012. The effect of diagenesis and fluid migration on rare earth element distribution in pore fluids of the northern Cascadia accretionary margin. Chem. Geol. 291, 152-165.

Kingsbury, J.A., Miller, C.F., Wooden, J.L., Harrison, T.M., 1993. Monazite paragenesis and U-Pb systematics in rocks of the eastern Mojave Desert, California, U.S.A.: implications for thermochronometry. Chem. Geol. 110, 147-167.

Kisch, H.J., 1991. Illite crystallinity: recommendations on sample preparation, X-ray diffraction settings, and interlaboratory samples. J. Metamorph. Geol. 9, 665-670.

Knoper, M., Armstrong, R., Andreoli, M., Ashwal, L., 2000. The Steenkampskraal monazite vein: a subhorizontal stretching shear zone indicating extensional collapse of Namaqualand at 1033 Ma? J. Afr. Earth. Sci. 31, Issue Suppl.,, 38-39.

Lafargue, E., Marquis, F., Pillot, D., 1998. Rock-Eval 6 Applications in Hydrocarbon Exploration, Production, and Soil Contamination Studies. Rev. Inst. Fr. Pét. 53, 421-437.

Lazareva, E.V., Zhmodik, S.M., Prokopiev, A.V., Karmanov, N.S., Sergeenko, A.I., 2018. Nodular monazite from placers in the Kular Ridge (Arctic Siberia, Russia): Composition and age. Russian Geology and Geophysics 59, 1330-1347.

Le Corre, C., 1975. Analyse comparée de la cristallinité des micas dans le Briovérien et le Paléozoique centre-armoricains; zonéographie et structure d'un domaine épizonal. Bull. Soc. Geol. Fr. S7-XVII, 547-553.

Le Corre, C., Auvray, B., Ballèvre, M., Robardet, M., 1991. Le massif armoricain. Sci. géol. Bull. 44, 31-103.

Le Corre, C., Le Theoff, B., 1976. Zoneographie de la deformation finie, de la fabrique et du metamorphisme dans un segment de la chaine hercynienne armoricaine. Bull. Soc. Geol. Fr. S7-XVIII, 1435-1442.

Lee, J.H., Byrne, R.H., 1992. Examination of comparative rare earth element complexation behavior using linear free-energy relationships. Geochim. Cosmochim. Acta 56, 1127-1137.

Lee, J.H., ., Byrne, R.H., 1993. Complexation of trivalent rare earth elements (Ce, Eu, Gd, Tb, Yb) by carbonate ions. Geochim. Cosmochim. Acta 57, 295-302.

Lev, S.M., McLennan, S.M., Meyers, W.J., Hanson, G.N., 1998. A petrographic approach for evaluating trace-element mobility in a black shale. J. Sediment. Res. 68, 970-980.

Lipin, B.R., McKay, G.A., 1989. Geochemistry and mineralogy of rare earth elements. Mineralogical Society of America, Washington, DC, US.

Liu, X., Byrne, R.H., 1997. Rare earth and yttrium phosphate solubilities in aqueous solution. Geochim. Cosmochim. Acta 61, 1625-1633.

Lulzac, Y., 1969. Contribution à la recherche et à l'étude des gîtes primaires de monazite grise à europium dans le massif armoricain. BRGM, DRMM 69.06, p. 41.

März, C., Poulton, S.W., Beckmann, B., Küster, K., Wagner, T., Kasten, S., 2008. Redox sensitivity of P cycling during marine black shale formation: Dynamics of sulfidic and anoxic, non-sulfidic bottom waters. Geochim. Cosmochim. Acta 72, 3703-3717.

Matys Grygar, T., Mach, K., Martinez, M., 2019. Checklist for the use of potassium concentrations in siliciclastic sediments as paleoenvironmental archives. Sediment. Geol. 382, 75-84.

McLennan, S.M., 2001. Relationships between the trace element composition of sedimentary rocks and upper continental crust. Geochem. Geophys. Geosyst. 2, n/a-n/a.

Merriman, R.J., Frey, M., 1999. Patterns of Very Low-Grade Metamorphism in Metapelitic Rocks, in: Frey, M., Robinson, D. (Eds.), Low-Grade Metamorphism. Blackwell Science, Oxford, pp. 61-107.

Merriman, R.J., Peacor, D.R., 1999. Very low-grade metapelites: mineralogy, microfabrics and measuring reaction progress, in: Frey, M., Robinson, D. (Eds.), Low-Grade Metamorphism. Blackwell Science, Oxford, pp. 10-60.

Merriman, R.J., Roberts, B., Peacor, D.R., 1990. A transmission electron microscope study of white mica crystallite size distribution in a mudstone to slate transitional sequence, North Wales, UK. Contrib. Mineral. Petrol. 106, 27-40.

Merriman, R.J., Roberts, B., Peacor, D.R., Hirons, S.R., 1995. Strain-related differences in the crystal growth of white mica and chlorite: a TEM and XRD study of the development of metapelitic microfabrics in the Southern Uplands thrust terrane, Scotland. J. Metamorph. Geol. 13, 559-576.

Michard, A., 1989. Rare earth element systematics in hydrothermal fluids. Geochim. Cosmochim. Acta 53, 745-750.

Milodowski, A.E., Zalasiewicz, J.A., 1991. Redistribution of rare earth elements during diagenesis of turbidite/hemipelagite mudrock sequences of Llandovery age from central Wales. Geol. Soc. London Spec. Publ. 57, 101.

Moëlo, Y., Rouer, O., Bouhnik-Le Coz, M., 2008. From diagenesis to hydrothermal recrystallization: polygenic Sr-rich fluorapatite from the oolitic ironstone of Saint-Aubin-des-Châteaux (Armorican Massif, France). Eur. J. Mineral. 20, 205-216.

Montel, J.-M., Foret, S., Veschambre, M., Nicollet, C., Provost, A., 1996. Electron microprobe dating of monazite. Chem. Geol. 131, 37-53.

Nance, R.D., Gutiérrez-Alonso, G., Keppie, J.D., Linnemann, U., Murphy, J.B., Quesada, C., Strachan, R.A., Woodcock, N.H., 2012. A brief history of the Rheic Ocean. Geosci. Front. 3, 125-135.

Noack, C.W., Dzombak, D.A., Karamalidis, A.K., 2014. Rare Earth Element Distributions and Trends in Natural Waters with a Focus on Groundwater. Environ. Sci. Technol. 48, 4317-4326.

Parrish, R.R., 1990. U–Pb dating of monazite and its application to geological problems. Can. J. Earth Sci. 27, 1431-1450.

Pepper, A.S., Corvi, P.J., 1995. Simple kinetic models of petroleum formation. Part I: oil and gas generation from kerogen. Mar. Pet. Geol. 12, 291-319.

Pochon, A., Gloaguen, E., Branquet, Y., Poujol, M., Ruffet, G., Boiron, M.-C., Boulvais, P., Gumiaux, C., Cagnard, F., Gouazou, F., Gapais, D., 2018. Variscan Sb-Au mineralization in Central Brittany (France): A new metallogenic model derived from the Le Semnon district. Ore Geol. Rev. 97, 109-142.

Poitrasson, F., Chenery, S., Bland, D.J., 1996. Contrasted monazite hydrothermal alteration mechanisms and their geochemical implications. Earth Planet. Sci. Lett. 145, 79-96.

Potel, S., Mählmann, R.F., Stern, W.B., Mullis, J., Frey, M., 2006. Very low-grade metamorphic evolution of pelitic rocks under high-pressure/low-temperature conditions, NW New Caledonia (SW Pacific). J. Petrol. 47, 991-1015.

Pourret, O., Davranche, M., Gruau, G., Dia, A., 2007. Rare earth elements complexation with humic acid. Chem. Geol. 243, 128-141.

Pourret, O., Tuduri, J., 2017. Continental shelves as potential resource of rare earth elements. Sci. Rep. 7, 5857.

Rasmussen, B., Buick, R., Taylor, W.R., 1998. Removal of oceanic REE by authigenic precipitation of phosphatic minerals. Earth Planet. Sci. Lett. 164, 135-149.

Rasmussen, B., Muhling, J.R., 2007. Monazite begets monazite: evidence for dissolution of detrital monazite and reprecipitation of syntectonic monazite during low-grade regional metamorphism. Contrib. Mineral. Petrol. 154, 675-689.

Rasmussen, B., Muhling, J.R., 2009. Reactions destroying detrital monazite in greenschist-facies sandstones from the Witwatersrand basin, South Africa. Chem. Geol. 264, 311-327.

Read, D., Andreoli, M.A.G., Knoper, M., Williams, C.T., Jarvis, N., 2002. The degradation of monazite: Implications for the mobility of rare-earth and actinide elements during low-temperature alteration. Eur. J. Mineral. 14, 487-498.

Read, D., Cooper, D.C., McArthur, J.M., 1987. The composition and distribution of nodular monazite in the lower Palaeozoic rocks of Great Britain. Mineral. Mag. 51, 271-280.

Rillard, J., Pourret, O., Censi, P., Inguaggiato, C., Zuddas, P., Toulhoat, P., Gombert, P., Brusca, L., 2019. Behavior of rare earth elements in an aquifer perturbed by CO2 injection: Environmental implications. Science of The Total Environment 687, 978-990.

Robardet, M., Doré, F., 1988. The late Ordovician diamictic formations from southwestern Europe: North-Gondwana glaciomarine deposits. Palaeogeogr. Palaeoclimatol. Palaeoecol. 66, 19-31.

Robardet, M., Verniers, J., Feist, R., Paris, F., 1994. Le Paléozoïque anté-varisque de France, contexte paléogéographique et géodynamique. Géologie de la France 3, 3-31.

Rosenblum, S., Mosier, E.L., 1983. Mineralogy and occurrence of europium-rich dark monazite. U.S. Geol. Surv. Prof. Pap. 1181, 67.

Salgueiro, R., Inverno, C., de Oliveira, D.P.S., Guimarães, F., Lencastre, J., Rosa, D., 2020. Alluvial nodular monazite in Monfortinho (Idanha-a-Nova, Portugal): Regional distribution and genesis. J. Geochem. Explor. 210, 106444.

Schmidt, D., Schmidt, S.T., Mullis, J., Ferreiro Mählmann, R., Frey, M., 1997. Very low grade metamorphism of the Taveyanne formation of western Switzerland. Contrib. Mineral. Petrol. 129, 385-403.

Schmitz, M.D., Schoene, B., 2007. Derivation of isotope ratios, errors, and error correlations for U-Pb geochronology using 205Pb-235U-(233U)-spiked isotope dilution thermal ionization mass spectrometric data. Geochem. Geophys. Geosyst. 8.

Schulz, B., Brätz, H., Bombach, K., Krenn, E., 2007. In-situ Th-Pb dating of monazite by 266 nm laser ablation and ICP-MS with a single collector, and its control by EMP analysis. Z. Angew. Geol. 35, 377-392.

Seydoux-Guillaume, A.-M., Montel, J.-M., Bingen, B., Bosse, V., de Parseval, P., Paquette, J.-L., Janots, E., Wirth, R., 2012. Low-temperature alteration of monazite: Fluid mediated coupled dissolution–precipitation, irradiation damage, and disturbance of the U–Pb and Th–Pb chronometers. Chem. Geol. 330-331, 140-158.

Sonke, J.E., Salters, V.J.M., 2006. Lanthanide–humic substances complexation. I. Experimental evidence for a lanthanide contraction effect. Geochim. Cosmochim. Acta 70, 1495-1506.

Spear, F.S., Pyle, J.M., 2002. Apatite, Monazite, and Xenotime in Metamorphic Rocks. Rev. Mineral. Geochem. 48, 293-335.

Suire, P., Dabard, M.-P., Chauvel, J.-J., 1991. The Ordovician Red Beds of Brehec (Armorican Massif): a sedimentological study. Comptes Rendus - Academie des Sciences, Serie II 312, 721-727.

Tartèse, R., Poujol, M., Gloaguen, E., Boulvais, P., Drost, K., Košler, J., Ntaflos, T., 2015. Hydrothermal activity during tectonic building of the Variscan orogen recorded by U-Pb systematics of xenotime in the Grès Armoricain formation, Massif Armoricain, France. Mineral. Petrol. 109, 485-500.

Tera, F., Wasserburg, G.J., 1972. U-Th-Pb systematics in three Apollo 14 basalts and the problem of initial Pb in lunar rocks. Earth Planet. Sci. Lett. 14, 281-304.

Tomascak, P.B., Krogstad, E.J., Walker, R.J., 1996. U-Pb monazite geochronology of granitic rocks from Maine: implications for late Paleozoic tectonics in the Northern Appalachians. J. Geol. 104, 185-195.

Trautmann, F., Delfour, J., Fourniguet, J., Scanvic, J.Y., Dubreuil, G., Pivette, B., Prian, J.P., Militon, C., Manigault, B., 1984. Carte géol. France (1/50000), feuille Redon (420). BRGM, Orléans, France.

Trautmann, F., Donnot, M., Lemaire, D., Cagnet-Mawhin, M.P., 1987. Carte géol. France (1/50000), feuille Nozay (420). BRGM, Orléans, France.

Tuduri, J., Charles, N., Guyonnet, G., Melleton, J., Pourret, P., A, R., 2015. Projet ANR ASTER. Rapport de Tâche 4. Potentialité de stocks géologiques de terres rares en Europe et au Groenland. Rapport final. BRGM/RP-64910-FR, Orléans, France.

Tuduri, J., Pourret, O., Gloaguen, E., Gouin, J., Potel, S., Dörr, W., Colin, S., Chevillard, M., 2014. U-Pb age and geochemistry of authigenic monazites of the Armorican Massif. Implications for formation of monazite-(MREE) from paleozoic shales, 24ème Réunion des Sciences de la Terre, Pau, France, pp. 342-343.

van de Kamp, P.C., 2016. Potassium distribution and metasomatism in pelites and schists: how and when, relation to post-depositional events. J. Sediment. Res. 86, 683-711.

Van Hoozen, C.J., Gysi, A.P., Harlov, D.E., 2020. The solubility of monazite (LaPO4, PrPO4, NdPO4, and EuPO4) endmembers in aqueous solutions from 100 to 250 °C. Geochim. Cosmochim. Acta 280, 302-316.

Vermeesch, P., 2018. IsoplotR: A free and open toolbox for geochronology. Geosci. Front. 9, 1479-1493.

Vanderhaeghe, O., Laurent, O., Gardien, V., Moyen, J.-F., Gébelin, A., Chelle-Michou, C., Couzinié, S., Villaros, A., Bellanger, M., 2020. Flow of partially molten crust controlling construction, growth and collapse of the Variscan orogenic belt: the geologic record of the French Massif Central. Bull. Soc. Geol. Fr. 191, 25.

Vidal, O., Dubacq, B., 2009. Thermodynamic modelling of clay dehydration, stability and compositional evolution with temperature, pressure and H2O activity. Geochim. Cosmochim. Acta 73, 6544-6564.

von Eynatten, H., Tolosana-Delgado, R., Karius, V., Bachmann, K., Caracciolo, L., 2016. Sediment generation in humid Mediterranean setting: Grain-size and source-rock control on sediment geochemistry and mineralogy (Sila Massif, Calabria). Sediment. Geol. 336, 68-80.

Warr, L., Ferreiro Mählmann, R., 2015. Recommendations for Kübler index standardization. Clay Miner. 50, 283-286.

Warr, L.N., Rice, A.H.N., 1994. Interlaboratory standardization and calibration of day mineral crystallinity and crystallite size data. J. Metamorph. Geol. 12, 141-152.

Wilby, P.R., Page, A.A., Zalasiewicz, J.A., Milodowski, A.E., Williams, M., Evans, J.A., 2007. Syntectonic monazite in low-grade mudrocks: a potential geochronometer for cleavage formation? J. Geol. Soc. 164, 53-56.

Wilkin, R.T., Barnes, H.L., 1997. Formation processes of framboidal pyrite. Geochim. Cosmochim. Acta 61, 323-339.

Wing, B.A., Ferry, J.M., Harrison, T.M., 2003. Prograde destruction and formation of monazite and allanite during contact and regional metamorphism of pelites: petrology and geochronology. Contrib. Mineral. Petrol. 145, 228-250.

Wood, S.A., 1990. The aqueous geochemistry of the rare-earth elements and yttrium: 1. Review of available low-temperature data for inorganic complexes and the inorganic REE speciation of natural waters. Chem. Geol. 82, 159-186.

Yang, J., Torres, M., McManus, J., Algeo, T.J., Hakala, J.A., Verba, C., 2017. Controls on rare earth element distributions in ancient organic-rich sedimentary sequences: Role of post-depositional diagenesis of phosphorus phases. Chem. Geol. 466, 533-544.

Zhu, C., Rao, S., Hu, S., 2016. Application of illite crystallinity for paleo-temperature reconstruction: a case study in the Western Sichuan Basin, SW China. Carpathian Journal of Earth and Environmental Sciences 11, 599-608.